

1 **A Statistical Comparison of Cirrus Particle Size Distributions**
2 **Measured Using the 2D Stereo Probe During the TC⁴,**
3 **SPartICus, and MACPEX Flight Campaigns with Historical**
4 **Cirrus Datasets**

5
6 M. Christian Schwartz

7 Argonne National Laboratory, 9700 Cass Avenue, Bldg. 240, 6.A.15, Lemont, IL, 60439, United States

8
9 *Correspondence to:* M. Christian Schwartz (mcs45@byu.net)

10 **Abstract.** This paper addresses two straightforward questions. First, how similar are the statistics of cirrus particle
11 size distribution (PSD) datasets collected using the 2D Stereo (2D-S) probe to cirrus PSD datasets collected using
12 older Particle Measuring Systems (PMS) 2D Cloud (2DC) and 2D Precipitation (2DP) probes? Second, how similar
13 are the datasets when shatter-correcting post-processing is applied to the 2DC datasets? To answer these questions,
14 a database of measured and parameterized cirrus PSDs, constructed from measurements taken during the Small
15 Particles in Cirrus (SPartICus), Mid-latitude Airborne Cirrus Properties Experiment (MACPEX), and Tropical
16 Composition, Cloud, and Climate Coupling (TC⁴) flight campaigns is used.

17 Bulk cloud quantities are computed from the 2D-S database in three ways: first, directly from the 2D-S
18 data; second, by applying the 2D-S data to ice PSD parameterizations developed using sets of cirrus measurements
19 collected using the older PMS probes; and third, by applying the 2D-S data to a similar parameterization developed
20 using the 2D-S data itself. This is done so that measurements of the same cloud volumes by parameterized versions
21 of the 2DC and 2D-S can be compared with one another. It is thereby seen, given the same cloud field and given the
22 same assumptions concerning ice crystal cross-sectional area, density, and radar cross section, that the parameterized
23 2D-S and the parameterized 2DC predict similar distributions of inferred shortwave extinction coefficient, ice water
24 content, and 94 GHz radar reflectivity. However, the parameterization of the 2DC based on uncorrected data
25 predicts a statistically significant higher number of total ice crystals and a larger ratio of small ice crystals to large
26 ice crystals than does the parameterized 2D-S. The 2DC parameterization based on shatter-corrected data also
27 predicts statistically different numbers of ice crystals than does the parameterized 2D-S, but the comparison between
28 the two is nevertheless more favorable. It is concluded that the older data sets continue to be useful for scientific
29 purposes, with certain caveats, and that continuing field investigations of cirrus with more modern probes is
30 desirable.

31 1 Introduction

32 For decades, in situ ice cloud particle measurements have often indicated ubiquitous, high concentrations of
33 the smallest ice particles (Korolev et al., 2013a; Korolev and Field, 2015). If the smallest ice particles are indeed
34 always present in such large numbers, then their effects on cloud microphysical and radiative properties are
35 pronounced. For instance, Heymsfield et al. (2002) reported small particles' dominating total particle concentrations
36 (N_{TS}) at all times during multiple Tropical Rainfall Measuring Mission (TRMM) field campaigns, while Field
37 (2000) noted the same phenomenon in mid-latitude cirrus. Lawson et al. (2006) reported N_{TS} in mid-latitude cirrus
38 ranging from $\sim .2$ - 1 cm^{-3} and estimated that particles smaller than 50 microns were responsible for 99% of N_T , 69%
39 of shortwave extinction, and 40% of ice water content (IWC). From several representative cirrus cases, Gayet et al.
40 (2002) reported average N_{TS} as high as 10 cm^{-3} and estimated that particles having maximum dimensions smaller
41 than 15.8 microns resulted in about 38% of measured shortwave extinction; and Gayet et al. (2004) and Gayet et al.
42 (2006) estimated from a broader set of measurements that particles smaller than 20 microns accounted for about
43 35% of observed shortwave extinction. Garrett et al. (2003) estimated that small ice crystals, with equivalent radii
44 less than 30 microns, contributed in excess of 90% of total shortwave extinction during the NASA Cirrus Regional
45 Study of Tropical Anvils and Cirrus Layers-Florida Area Cirrus Experiment (CRYSTAL-FACE).

46 While it is quite possible for relatively high numbers of small ice crystals to occur naturally (see, e.g., Zhao
47 et al., 2011; and Heymsfield et al., 2017), it is also possible for small ice particle concentrations to be significantly
48 inflated by several measurement artifacts. The various particle size distribution (PSD) probes (also known as single
49 particle detectors) in use employ a handful of different measurement techniques to detect and size particles across a
50 variety of particle size ranges. The units of a PSD are number of particles per unit volume per unit size. Thus, after
51 a PSD probe counts the particles that pass through its sample area, each particle is assigned a size as well as an
52 estimate of the sample volume from which it was drawn (Brennguier et al., 2013). Uncertainty in any of these PSD
53 components results in uncertain PSD estimates.

54 Leaving aside technologies still under development and test, such as the holographic detector of clouds
55 (HOLODEC; Fugal and Shaw, 2009), PSD probes fall into three basic categories: impactor probes, light scattering
56 probes, and imaging probes. (More thorough discussions on this topic, along with comprehensive bibliographies,
57 may be found in Brennguier et al., 2013, and in Baumgardner et al., 2017.) The earliest cloud and precipitation
58 particle probes were of the impactor type (Brennguier et al., 2013). Modern examples include the Video Ice Particle

59 Sampler (VIPS) (Heymsfield and McFarquhar, 1996), designed to detect particles in the range 5-200 μm . The basic
60 operating principle is thus: cloud and precipitation particles impact upon a substrate, leaving an imprint (or leaving
61 the particle itself) to be replicated (in the case of the VIPS, by digital imaging) and analyzed. This type of probe is
62 particularly useful for imaging the smallest ice crystals (Baumgardner et al., 2011; Brenguier et al., 2013).

63 Light scattering probes also are designed for detecting small, spherical and quasi-spherical particles (a
64 typical measurement range would be 1-50 μm ; see Baumgardner et al., 2017). These work by measuring, at various
65 angles, the scatter of the probe's laser due to the presence of a particle within the probe's sample area. Assuming
66 that detected particles are spherical and assuming their index of refraction, Mie theory is then inverted to estimate
67 particle size. Two prominent examples of this type of probe are the Forward Scattering Spectrometer Probe (FSSP;
68 Knollenberg, 1976, 1981) and the Cloud Droplet Probe (CDP; Lance et al., 2010).

69 Imaging probes, also known as optical array probes (OAPs), use arrays of photodetectors to make two-
70 dimensional images of particles that pass through their sample areas. Unlike the light scattering probes, OAPs make
71 no assumptions regarding particle shape or composition (Baumgardner et al., 2017), and they have broader
72 measurement ranges aimed both at cloud and precipitation particles. Two prominent examples are the Two-
73 Dimensional Stereo (2D-S; Lawson et al., 2006) probe, whose measurement range is 10-1280 μm , and the Two-
74 Dimensional Cloud (2DC; Knollenburg, 1976) probe, whose measurement range is 25-800 μm . OAPs designed for
75 precipitation particle imaging include the Precipitation Imaging Probe (PIP; Baumgardner et al., 2001) and the High
76 Volume Precipitation Spectrometer (HVPS; Lawson et al., 1998), which measure particles ranging from $\sim 100 \mu\text{m}$
77 up to several millimeters.

78 Because an estimate of the sample volume from which a particle is drawn is a function of the particle's size
79 and assumes that the particle is spherical (Brenguier et al., 2013), all PSD probes suffer from sample volume
80 uncertainty. Estimated sample volumes from OAPs perform suffer from the problem of sizing aspherical particles
81 from 2D images (see Fig 5-40, Brenguier et al., 2013). Nonetheless, impactor and light scattering probes both suffer
82 from much smaller sample volumes than do OAPs (Brenguier et al., 2013; Baumgardner et al., 2017; Heymsfield et
83 al., 2017). Scattering probes, for example, need up to several times the sampling distance in cloud as OAPs to
84 produce a statistically significant PSD estimate (see Fig. 5-3, Brenguier et al., 2013).

85 The obvious difficulty in sizing small ice crystals with light scattering probes is the application of Mie
86 theory to nonspherical ice crystals. Probes such as the FSSP and CDP are therefore prone to undersizing ice crystals

87 [\(Baumgardner et al., 2011; Brenguier et al., 2013; Baumgardner et al., 2017\).](#)

88 [Imaging particles using an OAP requires no assumptions regarding particle shape or composition, but](#)
89 [sizing algorithms based on two-dimensional images are highly sensitive to particle orientation \(Brenguier et al.,](#)
90 [2013\). Other sizing uncertainties stem from imperfect thresholds for significant occultation of photodiodes, the lack](#)
91 [of an effective algorithm for bringing out-of-focus ice particles into focus, and the use of statistical reconstructions](#)
92 [of partially imaged ice crystals that graze a probe's sample area \(Brenguier et al., 2013; Baumgardner et al., 2017\).](#)

93 [Ideally, PSDs estimated using different probes would be stitched together in order to provide a complete](#)
94 [picture of the ice particle population, from micron-sized particles through snowflakes \(Brenguier et al., 2013\).](#)

95 [However, while data from VIPS, fast FSSP, and Small Ice Detector-3 \(SID-3; Ulanowski et al., 2014\) probes are](#)
96 [available to complement the OAP data used in this study, none of them are used on account of sizing uncertainties](#)
97 [stemming from their small sample volumes and from spherical particle assumptions. The two publications](#)
98 [wherewith comparison is made in this paper also restricted their datasets to OAPs.](#)

99 [The main, remaining source of small particle counting and sizing dealt with in this study is particle](#)
100 [shattering. Shattering](#) of ice particles on probe tips and inlets and on aircraft wings has rendered many historical
101 cirrus datasets suspect (Vidaurre and Hallet, 2009; Korolev et al., 2011; [Baumgardner et al., 2017](#)) due to such
102 shattering's artificially inflating measurements of small ice particle concentrations (see, e.g., McFarquhar et al.,
103 2007; Jensen et al., 2009; and Zhao et al., 2011). Measured ice particle size distributions (PSDs) are used to
104 formulate parameterizations of cloud processes in climate and weather models, so the question of the impact of
105 crystal shattering on the historical record of ice PSD measurements is one of significance (Korolev and Field, 2015).

106 Post-processing of optical probe data based on measured particle inter-arrival times (Cooper, 1978; Field et
107 al., 2003; Field et al., 2006; Lawson, 2011; Jackson et al., 2014; Korolev and Field, 2015) has become a tool for
108 ameliorating contamination from shattered artifacts. Shattered particle removal is based on modeling particle inter-
109 arrival times by a Poisson process, assuming that each inter-arrival time is independent of all other inter-arrival
110 times. Jackson and McFarquhar (2014) posit that particle clustering (Hobbs and Rangno, 1985; Kostinski and Shaw,
111 2001; Pinsky and Khain, 2003; Khain et al., 2007), which would violate this basic assumption, is not likely a matter
112 of significant concern as cirrus particles are naturally spread further apart than [are](#) liquid droplets and sediment over
113 a continuum of size-dependent speeds.

114 [In addition, a posteriori shattered particle removal should be augmented with design measures such as](#)

115 specialized probe arms and tips (Vidaurre and Hallet, 2009; Korolev et al., 2011; Korolev et al., 2013a; Korolev and
116 Field, 2015). Probes must also be placed away from leading wing edges (Vidaurre and Hallet, 2009; Jensen et al.,
117 2009), as many small particles generated by shattering on aircraft parts are likely not be filtered out by shatter-
118 recognition algorithms.

119 The ideal way to study the impact of both shattered particle removal and improved probe design is to fly
120 two versions of a probe—one with modified design and one without—side by side and then to compare results from
121 both versions of the probe both with and without shattered particle removal. Results from several flight legs made
122 during three field campaigns where this was done are described in three recent papers: Korolev et al. (2013b),
123 Jackson and McFarquhar (2014), and Jackson et al. (2014). Probes built for several particle size ranges were
124 examined, but those of interest here are the 2D-S and the older 2DC. Three particular results distilled from those
125 papers are useful here.

126 First, [in agreement with Lawson \(2011\)](#), a posteriori shattered particle removal is more effective at
127 reducing counts of apparent shattering fragments for the 2D-S than are modified probe tips. The opposite is true for
128 the 2DC. This is attributed to the 2D-S' larger sample volume, [its](#) improvements in resolution and [electronic](#) time
129 response over the 2DC, [and to its 256 photodiode elements \(Jensen et al., 2009; Lawson, 2011; Brenguier et al.,](#)
130 [2013\)](#), which allow it to size particles smaller than 100 μm and to measure particle inter-arrival times more
131 accurately (Lawson et al., 2010; Korolev et al., 2013b; [Brenguier et al., 2013](#)).

132 Second, shattered artifacts seem mainly to corrupt particle size bins less than about 500 microns ([see also,](#)
133 [Baumgardner et al., 2011](#)). Thus Korolev et al. (2013b) posit that bulk quantities computed from higher order PSD
134 moments, such as shortwave extinction coefficient, IWC, and radar reflectivity, are likely to compare much better
135 between the 2D-S and the 2DC than is N_T ([see also, Jackson and McFarquhar, 2014; Heymsfield et al., 2017](#)).

136 Third, the efficacy of shattered particle removal from the 2DC is questionable: [the](#) post-processing is prone
137 to accepting shattered particles and to rejecting real particles (Korolev and Field, 2015). The parameters of the
138 underlying Poisson model and its ability to correctly identify shattered fragments depend on the physics of the cloud
139 being sampled (Vidaurre and Hallett, 2009; Korolev et al., 2011), [and the older 2DC experiences more issues](#) with
140 instrument depth-of-field, unfocused images, and image digitization [than do newer OAPs](#), further compounding
141 uncertainty [in the shattered particle removal](#) (Korolev et al., 2013b; Korolev and Field, 2015).

142 In the context of relatively small studies such as these, Korolev et al. (2013b) pose two questions: “(i) to

143 what extent can the historical data be used for microphysical characterization of ice clouds, and (ii) can the historical
144 data be reanalyzed to filter out the data affected by shattering?” One difficulty in addressing these questions is the
145 scarcity of data from side-by-side instrument comparisons. Another is that, especially for the 2DC, “correcting
146 [data] a posteriori is not a satisfactory solution” (Vidaurre and Hallet, 2009). However, shattered particle removal is
147 the main (if not the only) correction method available when revisiting historical datasets.

148 In order to address Korolev et al.’s (2013b) first question, bulk cloud properties derived from shatter-
149 corrected 2D-S data are used to answer two questions: 1) How similar are the statistics of cirrus PSD datasets
150 collected using the 2D-S probe to cirrus PSD datasets collected using older 2DC and 2DP probes? 2) How similar
151 are the datasets when shatter-correcting post-processing is applied to the 2DC datasets? In proceeding, two points
152 are critical to recall. First, the 2D-S is reasonably expected to give results superior to the 2DC after shattered
153 particle removal. Second, lingering uncertainty notwithstanding, results presented elsewhere from the shatter-
154 corrected 2D-S reveal behaviors in ice microphysics within different regions of cloud that are expected both from
155 physical reasoning and from modeling studies and that were not always discernible before from in situ datasets
156 (Lawson, 2011; Schwartz et al., 2014).

157 To this end, a substantial climatology of shatter-corrected, 2D-S-measured cirrus PSDs is indirectly
158 compared with two large collections of older datasets, collected from the early 1990s through the mid-2000s mainly
159 using Particle Measurement Systems 2DC and Two-Dimensional Precipitation (2DP) probes (Baumgardner, 1989)
160 as well as Droplet Measurement Technologies Cloud- and Precipitation-Imaging Probes (CIP and PIP; Heymsfield
161 et al., 2009), and in one instance, the 2D-S. The older datasets are presented and parameterized in Delanoë et al.
162 (2005; hereinafter D05) and in Delanoë et al. (2014; hereinafter D14). The data used in D05 were not subject to
163 shattered particle removal, whereas the data in D14 were a posteriori.

164 The comparison strategy, in short is as follows. The D05/D14 parameterizations consist of normalized,
165 “universal” cirrus PSDs to which functions of PSD moments are applied as inputs. The results of so doing are sets
166 of parameterized 2DC PSDs—both shatter-corrected and uncorrected. To make the comparison, the same moments
167 from 2D-S-measured PSDs are applied to the D05/D14 parameterizations in order to simulate what the shatter- and
168 non-shatter-corrected 2DCs would have measured had they flown with the 2D-S. Then, a “universal” PSD derived
169 from the 2D-S itself is computed in order to make a fair comparison. The moments from the 2D-S-measured PSDs
170 are applied to the 2D-S “universal” PSD and it is then seen whether the older datasets differ statistically from the

171 | newer [in their](#) derived cirrus bulk properties. [This procedure is illustrated in Fig. 1.](#)

172 | Section 2 contains a description of the data used herein. Section 3 discusses the fitting of PSDs with
173 | gamma distributions for computational use, Section 4 discusses the normalization and parameterization schemes
174 | used by D05/D14, and Section 5 discusses the effects of not having included precipitation probe data with the 2D-S
175 | data. Section 6 demonstrates the final results of the comparison [and concludes with a discussion.](#)

176 | **2 Data**

177 | The 2D-S data was collected during the Mid-Latitude Airborne Cirrus Experiment (MACPEX), based in
178 | Houston, TX during February and March, 2011 (MACPEX Science Team, 2011); the Small Particles in Cirrus
179 | (SPartICus) campaign, based in Oklahoma during January through June, 2010 (SPartICus Science Team, 2010); and
180 | TC⁴, based in Costa Rica during July, 2007 (TC⁴ Science Team, 2007). The SPEC 2D-S probe (Lawson, 2011)
181 | images ice crystal cross-sections via two orthogonal lasers that illuminate two corresponding linear arrays of 128
182 | photodiodes. PSDs, as well as distributions of cross-sectional area and estimated mass, are reported every second in
183 | 128 size bins with centers starting at 10 microns and extending out to 1280 microns. Particles up to about three
184 | millimeters can be sized in one dimension by recording the maximum size along the direction of flight. During
185 | SPartICus the 2D-S flew aboard the SPEC Inc. Learjet, while during MACPEX it was mounted on the NASA WB57
186 | aircraft. During TC⁴ it was mounted on both the NASA DC8 and the NASA WB57, but the WB57 data is not used
187 | due to documented contamination of the data from shattering artifacts off of the aircraft wing (Jensen et al., 2009).

188 | Temperature was measured during MACPEX, TC⁴, and SPartICus using a Rosemount total temperature
189 | probe. Bulk IWC measurements are available for MACPEX from the Closed-path tunable diode Laser Hygrometer
190 | (CLH) probe (Davis et al., 2007). Condensed water that enters the CLH is evaporated so that a measurement of total
191 | water can be made. The condensed part of the total water measured by the CLH is obtained by estimating
192 | condensed water mass from concurrent PSDs measured by the National Center for Atmospheric Research (NCAR)
193 | Video Image Particle Sampler (VIPS) probe and then subtracting this estimate from the measured total water mass.

194 | **3 Parametric Fitting of PSDs**

195 | PSDs measured by the 2D-S were fit with both unimodal and bimodal parametric gamma distributions.

196 | The unimodal distribution is

$$197 | n(D) = N_0 \left(\frac{D}{D_0} \right)^\alpha \exp\left(-\frac{D}{D_0} \right), \quad (1)$$

198 where D is particle maximum dimension, D_0 is the scale parameter, α is the shape parameter, and N_0 is the so-called
199 intercept parameter. The bimodal distribution is simply a mixture of two unimodal distributions:

$$200 \quad n(D) = N_{01} \left(\frac{D}{D_{01}} \right)^{\alpha_1} \exp\left(-\frac{D}{D_{01}}\right) + N_{02} \left(\frac{D}{D_{02}} \right)^{\alpha_2} \exp\left(-\frac{D}{D_{02}}\right). \quad (2)$$

201 Save in a handful of instances (which will be indicated), all bulk PSD quantities shown here are computed using
202 these parametric fits. A combination of unimodal and bimodal fits is used to compute N_T , dictated by the shape of
203 the PSD as determined by a generalized chi-squared goodness of fit test (Schwartz., 2014). Unimodal fits are used
204 to compute all other bulk quantities.

205 Unimodal fits were performed via the method of moments [in a manner similar to Heymsfield et al.
206 (2002)]. Both the method of moments and an expectation maximization algorithm (Moon, 1996; Schwartz, 2104)
207 were used for the bimodal fits; the more accurate of those two fits [as determined by whether fit provided the
208 smaller binned Anderson-Darling test statistic (Demortier, 1995)] being kept.

209 Measured PSDs are both truncated and time-averaged in order to mitigate counting uncertainties. It is here
210 assumed that temporal averaging sufficiently reduces Poisson counting noise so that it may be ignored [see, e.g.,
211 Gayet et al. (2002)]. Given already cited concerns regarding uncertainty in shattered particle removal, the smallest
212 size bins are not automatically assumed here to be reliable. Other competing uncertainties further complicate
213 particle counts within the first few size bins, e.g., [decreased detection efficiency within the first size bin](#)
214 [\(Baumgardner et al., 2017\)](#), the possible underestimation of counts of real particles by a factor of 5-10 (Gurganus
215 and Lawson, 2016), and mis-sizing of larger [particles](#) into smaller size bins due to image break-up at the edge of the
216 instrument's depth of field (Korolev et al., 2013b; Korolev and Field, 2015; [Baumgardner et al., 2017](#)).

217 In order to determine how many of the smallest size bins to truncate and for how many seconds to average
218 in order to make the counting assumption valid, two simple exercises were performed using the MACPEX dataset.
219 In the first exercise, fifteen-second temporal averages were performed along with truncating zero through two of the
220 smallest size bins while only the unimodal fits (chosen according to a maximum likelihood ratio test [Wilks, 2006])
221 were kept. [This exercise was performed first so as to prevent the most spurious size bins' interfering with the](#)
222 [smoothing out of Poisson counting noise](#). Figure 2 shows comparisons of distributions of measured and computed
223 (from the fits) N_T s. The difference in the number of samples of computed N_T between zero bins and one bin
224 truncated is an order of magnitude higher than that between one bin and two bins truncated. This is due to frequent,

225 extraordinarily high numbers of particles recorded in the smallest size bin that at times cause a PSD to be flagged as
226 bimodal by the maximum likelihood ratio test. As this effect lessens greatly after truncating only one bin, and as the
227 computed and measured N_{TS} are otherwise better matched using a single-bin truncation, the smallest size bin is
228 ignored for all PSDs (making the smallest size bin used 15-25 microns).

229 Also, IWC was estimated from the fit distributions (the first size bin having been left off in the fits) using
230 the mass-dimensional relationship $m(D) = 0.0065D^{2.25}$ (m denotes mass, and all units are cgs) given in
231 Heymsfield (2003) for mid-latitude cirrus. The distribution of IWC thus computed nominally matches (not shown)
232 IWC estimates from both the CLH and from the 2D-S data product, which uses mass-projected area relationships
233 (Baker and Lawson, 2006).

234 For the second exercise, temporal averages from one to 20 seconds were performed, truncating the first size
235 bin and again keeping only the unimodal fits. The balance to strike in picking a temporal average length is to
236 smooth out Poisson counting uncertainties acceptably without losing physical information to an overlong average.
237 Qualitatively, the statistics of the fit parameters begin to steady at around 15 seconds (not shown), so a fifteen-
238 second temporal average was chosen. Using the data filters, temporal average, and bin truncation thus far described
239 results in ~17 000 measured PSDs and their accompanying fits.

240 It must be noted that the first 2D-S size bin contains at least some real particles, though the afore-
241 mentioned uncertainties make it impossible (at present) to know how many. Therefore, N_{TS} computed from the
242 remaining bins can be underestimates. Parametric fits extrapolate the binned data all the way to size zero, though;
243 so it could be assumed, if the real ice particle populations are in fact gamma-distributed, that this extrapolation is a
244 fair estimate of the real particles lost due to truncating the first size bin. In truth, however, the assumption of a
245 gamma-shaped PSD is arbitrary, if convenient; but the gamma PSD shape is kept for its convenience and for its
246 ability to reproduce higher-order PSD moments. However, in this paper, where N_{TS} (equivalently, the zeroth
247 moments) from either the parametric, the binned, or the normalized parametric PSDs are computed, the
248 computations are begun at the left edge of the second size bin so as to compare equivalent quantities. In other
249 words, N_{TS} presented for comparison here are truncated to compensate for having left off the smallest size bin.

250 **4 Normalization and Parameterization**

251 In this section, the functions of 2D-S-measured PSD moments that are applied to the D05/D14
252 parameterizations (see Figure 1) are explained. However, the D05 and D14 parameterizations make use of PSDs in

253 terms of equivalent melted diameter D_{eq} . Before computing any moments, it is therefore necessary first to transform
 254 all 2D-S-measured PSDs from functions of maximum dimension D to functions of equivalent melted diameter D_{eq} .

255 Each 2D-S-measured PSD $n_D(D)$, whose independent variable is ice particle maximum dimension, is
 256 transformed to a distribution $n_{D_{eq}}(D_{eq})$ whose independent variable is equivalent melted diameter. The
 257 transformations are performed twice: once using the density-dimensional relationship used in D05 and once using a
 258 mass-dimensional relationship used in D14. The first transformation allows for application of the 2D-S data to the
 259 D05 parameterization, and the second first transformation allows for application of the 2D-S data to the D14
 260 parameterization.

261 The density-dimensional relationship $\rho(D) = aD^b$ (ρ denotes density, D denotes particle maximum
 262 dimension, the power law coefficients are $a = 0.0056$ and $b = -1.1$, and all units are cgs) used in D05 stems
 263 from relationships published by Locatelli and Hobbs (1974) and Brown and Francis (1995) for aggregate particles.
 264 Setting masses equal as in D05 results in the independent variable transformation

$$265 \quad \underline{D_{eq} = \left(\frac{aD^b}{\rho_w} \right)^{1/3} D, (3)}$$

266 where ρ_w is the density of water.

267 The mass-dimensional relationship labeled “Composite” (Heymsfield et al., 2010) in D14 is used here for
 268 the second transformation:

$$269 \quad \underline{m(D) = 7e^{-3}D^{2.2} = a_m D^{b_m} .}$$

270 (Here, m denotes mass, the power law coefficients are $a_m = 7e^{-3}$ and $b_m = 2.2$, and all units are cgs.) Setting
 271 masses equal results in the independent variable transformation

$$272 \quad \underline{D_{eq} = \left(\frac{6a_m}{\pi\rho_w} \right)^{1/3} D^{b_m/3} . (4)}$$

273 The “Composite” relation was only used to normalize about 54% of the PSDs utilized in D14; however, those

274 datasets so normalized are broadly similar to MACPex, SPARTICUS, and TC⁴ (one in fact is TC⁴, where the Cloud
 275 Imaging Probe was used as well as the 2D-S), and so the “Composite” relation is used here for comparison with
 276 D14.

277 Following D05/D14s’ notation, transformed PSDs then have their independent variable scaled by mass-
 278 mean diameter

$$279 \quad D_m = \frac{\int_0^\infty D_{eq}^4 n_{D_{eq}}(D_{eq}) dD_{eq}}{\int_0^\infty D_{eq}^3 n_{D_{eq}}(D_{eq}) dD_{eq}} \quad (5)$$

280 and their ordinates scaled by

$$281 \quad N_0^* = \frac{4^4 \left[\int_0^\infty D_{eq}^3 n_{D_{eq}}(D_{eq}) dD_{eq} \right]^5}{\Gamma(4) \left[\int_0^\infty D_{eq}^4 n_{D_{eq}}(D_{eq}) dD_{eq} \right]^4}, \quad (6)$$

282 so that

$$283 \quad n_{D_{eq}}(D_{eq}) = N_0^* F\left(x = \frac{D_{eq}}{D_m}\right). \quad (7)$$

284 In Eq. (7), $F(x)$ is, ideally, the universal, normalized PSD (Meakin, 1992; Westbrook et al., 2004a,b; D05; Tinel

285 et al, 2005; D14). The quantities N_0^* and D_m are the functions of 2D-S-measured PSD moments that are required

286 for application to the D05/D14 parameterizations in order to produce parameterized, corrected and uncorrected 2DC

287 PSDs (see Figure 1). The procedure for transforming and normalizing the 2D-S-measured PSDs and for computing

288 N_0^* and D_m is now explained.

289 Starting with binned PSDs, the normalization procedure is wended as described in section 4.1 of D05.

290 First, the 2D-S bin centers and bin widths are transformed once using Eq. (3) for the comparison with D05 and once

291 again using Eq. (4) for the comparison with D14. Next, each binned PSD is transformed by scaling from D -space to

292 D_e -space (see below). Then, via numerically computed moments, Eqs. (5)-(7) are used to produce one N_0^* , D_m

293 pair for each measured PSD and to normalize the binned, mass-equivalent spherical PSDs, which are then grouped

294 into normalized diameter bins of $\Delta x = 0.10$.

295 The scale factor for transforming binned PSDs is derived using this simple consideration: if the number of
296 particles within a size bin is conserved upon the bin's transformation from D -space to D_e -space, then, given that the
297 transformation is from maximum dimension to mass-equivalent spheres, so also is the mass of the particles within a
298 size bin conserved. That is,

$$299 \quad n_{D_{eq}}(D_{eq_i}) = n_D(D_i) \frac{a D_i^{b+3} \Delta D_i}{\rho_w D_{eq_i}^3 \Delta D_{eq_i}} \quad (8)$$

300 for the D05 transformation and

$$301 \quad n_{D_{eq}}(D_{eq_i}) = n_D(D_i) \frac{a_m D_i^{b_m} \Delta D_i}{\left(\frac{\pi}{6}\right) \rho_w D_{eq_i}^3 \Delta D_{eq_i}} \quad (9)$$

302 for the D14 transformation. (The subscript i is iterated through each size bin.)

303 Mass-equivalent transformations theoretically ensure that both N_T and IWC can be obtained by using the
304 PSD in either form:

$$305 \quad N_T = \int_0^\infty n_D(D) dD = \int_0^\infty n_{D_{eq}}(D_{eq}) dD_{eq} \quad (10)$$

$$306 \quad IWC = \frac{\pi}{6} \int_0^\infty a D^{b+3} n_D(D) dD = \frac{\pi}{6} \int_0^\infty \rho_w D_{eq}^3 n_{D_{eq}}(D_{eq}) dD_{eq} \quad (11a), \text{ or}$$

$$307 \quad IWC = \int_0^\infty a_m D^{b_m} n_D(D) dD = \frac{\pi}{6} \int_0^\infty \rho_w D_{eq}^3 n_{D_{eq}}(D_{eq}) dD_{eq} \quad (11b)$$

311 (Whether Eq. (11a) or Eq. (11b) is used depends upon whether the D05 or the D14 transformation is being
312 considered.) As it turns out, scaling from D -space to D_{eq} -space so that Eqs. (10) and (11) are both satisfied is not
313 necessarily possible. Since for the sake of estimating $\underline{D_m}$ and $\underline{N_0^*}$ it is more important that IWCs be matched, this
314 was done for the D05 comparison while matching the N_T s to within a factor of approximately 0.75, plus a bias of
315 $\sim 3.1 \text{ L}^{-1}$.

316 The following transformation of variables must be used for computing other bulk quantities from

317 transformed PSDs (Bain and Englehardt, 1992):

318
$$n_D(D) = n_{D_{eq}} \left[D_{eq}(D) \right] \left| \frac{dD_{eq}}{dD} \right|^{-1}. \quad (12)$$

319 For instance, effective radar reflectivity is computed [by integrating over particle maximum dimension intervals](#),
320 using a set of [particle maximum dimension/backscatter power-laws that were fit piecewise from](#) T-matrix
321 computations of backscatter cross section to particle maximum dimension (Matrosov, 2007; Matrosov et al., 2012;
322 Posselt and Mace, 2013; Hammonds et al., 2014) as follows:

323
$$Z_e = \frac{10^8 \lambda^4}{|K_w|^2 \pi^5} \sum_j \int_{D_j}^{D_{j+1}} a_{zj} D^{b_{zj}} n_{D_{eq}} \left[D_{eq}(D) \right] \left| \frac{dD_{eq}}{dD} \right| dD$$

324 The [set of power law](#) coefficients (a_{zj}, b_{zj}) [was](#) derived assuming an air/ice dielectric mixing model and that all
325 particles are prolate spheroids with aspect ratios of 0.7 (Korolev and Isaac, 2003; Westbrook et al., 2004a;
326 Westbrook et al., 2004b; Hogan et al., 2012). Several explicit expressions for computing bulk quantities based on
327 equivalent distributions may be found in Schwartz (2014).

328 In D05/D14, data taken with cloud particle and precipitation probes were combined to give PSDs ranging
329 from 25 μm to several millimeters. No precipitation probe data is used here, but how does not including
330 precipitation probe data affect the comparison? This question will be addressed later in this paper.

331 Two-dimensional histograms of the normalized PSDs are shown in Fig. [3](#) for the D05 transformation and in
332 Fig. [5](#) for the D14 transformation, overlaid with their mean normalized PSDs (cf. Figs. 1 and 2 in D05 and Fig. 3 in
333 D14). For both transformations, the mean normalized PSDs for the three datasets combined are repeated in Figs. [4](#)
334 and [6](#) as solid curves (cf. Fig. 3 of D05 and Fig. 6 of D14). These serve as the empirical universal, normalized PSDs

335 $F_{\sim 2DS-D05}(x)$ and $F_{\sim 2DS-D14}(x)$, derived using the mass transformations of D05 and D14, respectively. They,
336 and the quantities derived therefrom, serve to [parameterize](#) the more modern 2D-S with shattered particle removal.

337 The subscripts $\sim 2DS-D05$ and $\sim 2DS-D14$ are used hereinafter to represent bulk quantities derived using

338 $F_{\sim 2DS-D05}(x)$ and $F_{\sim 2DS-D14}(x)$.

339 Three parametric functions for $F(x)$ are given in D05, two of which are repeated here: the gamma- μ

340 function (F_μ) and the modified gamma function ($F_{\alpha,\beta}$; Petty and Huang, 2011).

$$341 \quad F_\mu(x) = \frac{\Gamma(4)(4+\mu)^{4+\mu}}{4 \Gamma(4+\mu)} x^\mu \exp[-(4+\mu)x] \quad (13)$$

$$342 \quad F_{\alpha,\beta}(x) = \beta \frac{\Gamma(4) \Gamma\left(\frac{\alpha+5}{\beta}\right)^{4+\alpha}}{4^4 \Gamma\left(\frac{\alpha+4}{\beta}\right)^{5+\alpha}} x^\alpha \exp\left[-\left(\frac{\Gamma\left(\frac{\alpha+5}{\beta}\right)}{\Gamma\left(\frac{\alpha+4}{\beta}\right)}\right)^\beta\right] \quad (14)$$

343 Values of μ , α , and β can be chosen to fit these functions to a mean normalized PSD. In D05, the parametric

344 functions $F_{\alpha,\beta} = F_{(-1,3)}$ (Eq. (14)) and $F_\mu = F_3$ (Eq. (13)) are given to approximate the universal PSD derived

345 from combined 2DC-2DP datasets; and in D14, the parametric function $F_{\alpha,\beta} = F_{(-0.262,1.754)}$ is given to

346 approximate the universal PSD derived from shatter-corrected datasets collected mainly with combined 2DC-2DP

347 probes.

348 These functions are used to parameterize transformed PSDs measured by the 2DC-2DP, given N_0^* and

349 D_m . We therefore make the assumption that if we take N_0^* and D_m derived from a 2D-S-measured PSD and then

350 apply them to Eq. (13) or (14), we have effectively simulated the parameterized, transformed PSD that a combined

351 2DC-2DP would have observed had they been present with the 2D-S. The subscripts $\sim 2DCu$ and $\sim 2DCs$ are used

352 hereinafter to represent quantities that simulate 2DC-2DP data (non-shatter-corrected and shatter-corrected,

353 respectively) in this way. Thus, we begin with two versions of $F_{\sim 2DCu}(x) = F_\mu = F_3$ and $F_{\alpha,\beta} = F_{-1,3}$ —and

354 one version of $F_{\sim 2DCs}(x) = F_{\alpha,\beta} = F_{(-0.262,1.754)}$ —Initial observations on comparison of $F_{\sim 2DS-D05}(x)$ and

355 $F_{\sim 2DS-D14}(x)$ with $F_{\sim 2DCu}(x)$ and $F_{\sim 2DCs}(x)$ will now be given.

356 4.1 Comparison with D05

357 Some important qualitative observations can be made from examining $F_{\sim 2DS-D05}(x)$ in Fig. 4. First, in

358 contrast to Fig. 3 of D05, the concentrations of particles at the smallest scaled diameters of $F_{\sim 2DS-D05}(x)$ are, on

359 | average, about an order of magnitude or more lower [than for the mean, normalized PSD in D05](#). From this it is
 360 | surmised that while the 2D-S continues to register relatively high numbers of small ice particles, the number has
 361 | decreased in the newer datasets due to the exclusion of [larger numbers of](#) shattered ice crystals.

362 | It can also be seen in Fig. 4 that the shoulder in the normalized PSDs in the vicinity of $x \sim 1.0$ exists in the
 363 | newer data as it does in the data used in D05. It is worth noting, though, that the shoulder exists in the one tropical
 364 | dataset used here (TC⁴), whereas it is absent or much less noticeable in the tropical datasets used in D05.

365 | Fortuitously, $F_{\alpha,\beta} = F_{(-1,3)}$ fits the 2D-S data better than it does the older data [in D05](#) at the smallest
 366 | normalized sizes (cf. Fig. 2 in D05). Neither $F_{\alpha,\beta} = F_{(-1,3)}$ nor $F_{\mu} = F_3$ correctly catches the shoulder in the
 367 | newer data, though $F_{\alpha,\beta} = F_{(-1,3)}$ was formulated to (better) catch a corresponding shoulder in the older data.

368 | Next, a comparison of PSD quantities computed directly from the 2D-S with corresponding $\sim 2DC$ -derived
 369 | quantities (computed using N_0^* and D_m derived directly from the binned 2D-S data and applied to $F_{\alpha,\beta} = F_{(-1,3)}$

370 | and $F_{\mu} = F_3$) is made. The extinction coefficient, IWC, and 94 GHz radar reflectivity compare well between the
 371 | 2D-S and both versions of $\sim 2DCu$ (not shown). As for N_T , it is the least certain computation (see Fig. 7); but

372 | $F_{\mu} = F_3$ is entirely wrong in attempting to reproduce this quantity, so this shape is not used hereinafter and

373 | $F_{\sim 2DCu}(x) = F_{(-1,3)}(x)$ is the shape used to simulate the uncorrected 2DC-2DP.

374 | Figure 8 shows the mean relative error and the standard deviation of the relative error (cf. Fig. 5 of D05)
 375 | between 2D-S-derived and corresponding $\sim 2DCu$ -derived quantities. Effective radius is as defined in D05. Mean
 376 | relative error for both extinction coefficient and IWC is about -0.1%. The mean relative error in N_T (N_T computed
 377 | directly from [truncated](#), binned PSDs is used both here and in Fig. 9) is rather large at $\sim 50\%$; and the mean relative
 378 | error in Z_e , at $\sim 22\%$, is larger than that shown in Fig. 5 of D05 (less than 5% there) but, at about 2 dB, is within the
 379 | error of most radars. This may well be due to the overestimation of $F(x)$ by $F_{\sim 2DCu}(x)$ between normalized

380 | sizes of about 1.2 and 2 [see Fig. 4b]. Both here and in D05, $F_{\sim 2DCu}(x)$ falls off much more rapidly than

381 | $F_{\sim 2DS-D05}(x)$ above a normalized diameter of two. However, it is deduced from Figs. 2 and 5 in D05 that this

382 roll-off is not responsible for the large mean relative error in Z shown in Fig. 8.

383 The mean relative error in effective radius shown in Fig. 8 is approximately -7%, whereas it is apparently
384 nil in Fig. 5 of D05. Effective radius is defined in D05 as the ratio of the third to the second moments of the
385 spherical-equivalent PSDs and is therefore a weighted mean of the PSD. The negative sign on the relative error
386 indicates that, on average, $F_{\sim 2DCu}(x)$ is underestimating the effective radius of the PSDs measured by the 2D-S
387 whereas for the older datasets it hits the effective radius spot-on (in the average). Therefore, there is a significant
388 difference between the 2D-S datasets and the older 2DC-2DP datasets in the ratio of large particles to small
389 particles, even when precipitation probe data is not combined with the 2D-S.

390 4.2 Comparison with D14

391 From Fig. 5, concentrations at the smallest scaled diameters of $F_{\sim 2DS-D14}(x)$ are nominally consistent
392 with those shown in Fig. 6 of D14. In accordance with the surmise made in the comparison with D05 above, it
393 would seem that shattered particle removal from the 2DC improves comparison between the 2D-S and the 2DC-2DP
394 at the smallest particle sizes.

395 Here, $F_{\sim 2DCs}(x) = F_{(-0.262, 1.754)}(x)$. The shoulder in the normalized PSDs in the vicinity of $x \sim 1.0$ is
396 again found, though the shoulder is not captured by $F_{\sim 2DCs}(x)$ (see Fig. 6). The normalized 2D-S at the smallest
397 normalized sizes is also underestimated by $F_{\sim 2DCs}(x)$. Comparison of N_T computed using $F_{\sim 2DCs}(x)$ with that
398 derived from 2D-S is quite similar to that of $F_{\sim 2DCu}(x)$ (not shown).

399 As shown in Fig. 9, the mean relative error between N_T and effective radius derived from the 2D-S and
400 from $\sim 2DCs$ is again about 50%, while the mean relative error in effective radius remains about -7.5%. The mean
401 relative error in reflectivity has decreased to about 14%.

402 5 Impact of Not Using Precipitation Probe Data

403 To more formally investigate the impact of not using a precipitation probe, data from the PIP were
404 combined with data from the 2D-S using the TC⁴ dataset. This campaign of the three was chosen due to its tending
405 to occur at warmer temperatures, in a more convective environment, and at lower relative humidities: therefore, if
406 large particles are going to matter, they should matter for TC⁴. Figure 10 shows, similar to Figs. 4 and 6,

407 $F_{\sim 2DS-D05}(x)$ for the 2D-S alone, $F_{\sim 2DS/PIP-D05}(x)$ for the 2D-S combined with the PIP, and $F_{\sim 2DCu}(x)$.

408 In the combined data, $F_{\sim 2DS/PIP-D05}(x)$ does not dig as low between zero and unity as for the 2D-S alone;

409 but it does show similar numbers of particles at the very smallest normalized sizes, and the shoulder is in the same

410 location. Beginning at about $x = 1.2$, the 2D-S-PIP normalized distribution is higher than the 2D-S-alone

411 normalized distribution; and it continues out to about $x = 10$, whereas the 2D-S-alone distribution ends shy of $x = 5$.

412 In either case, $F_{\sim 2DCu}(x)$ misses what is greater than about $x = 2$. This roll-off, along with the fact that

413 $F_{\sim 2DS/PIP-D05}(x)$ appears to be more similar to $F_{\sim 2DS-D05}(x)$ than it does to $F_{\sim 2DCu}(x)$, indicate that a

414 parameterization of $F(x)$ based off the 2D-S alone is comparable to the 2DC/2DP-based $F_{\sim 2DCu}(x)$

415 parameterization.

416 In support of this assertion, Fig. 11 shows the penalty in radar reflectivity, computed directly from data

417 using the approach described earlier, incurred by using only the 2D-S instead of the 2D-S-PIP. The penalty is in the

418 neighborhood of 1 dB.

419 The true ([in the sense that they are derived directly from measurements](#)) N_0^* and D_m computed from each

420 of the 2D-S PSDs alone and from the combined PSDs from TC⁴ were used, along with $F_{\sim 2DCu}(x)$, to compute N_T ,

421 extinction coefficient, IWC, and 94 GHz effective radar reflectivity. This amounts to two different $\sim 2DCu$

422 simulations: one including the PIP and one not. The results are shown in Fig. 12. The distributions are very

423 similar, with the exception of the reflectivity distributions, whose means are separated by less than 1 dBZ. It is

424 concluded that the cloud filtering technique has resulted in PSDs that are satisfactorily described by the 2D-S alone,

425 at least in the case of this comparison.

426 6 Final Results and Discussion

427 In D05, complete parameterization of a 2DC-2DP-measured PSD is achieved by using [the](#) universal shape

428 $F_{\alpha,\beta}(x)$ along with N_0^* parameterized by radar reflectivity and D_m parameterized by temperature. For

429 comparison with the shattered-corrected D14 study, a temperature-based parameterization of “composite”-derived

430 D_m is also [computed](#) from the 2D-S data and “composite”-derived N_0^* is [also](#) parameterized by radar reflectivity.

431 A similar parameterization scheme (also based on radar reflectivity and temperature) for the 2D-S (based on Field et
432 al., 2005) is outlined in Schwartz (2014) and is used here to compute a fully parameterized version of 2D-S-
433 measured PSDs so as to make a fair comparison of them with fully parameterized 2DC-2DP-measured PSDs.

434 Figure 13 shows the results of computing PSD-based quantities using the fully parameterized 2D-S (red,
435 labeled “ $x2DS$ ”), the fully parameterized (uncorrected) 2DC-2DP (blue, labeled “ $x2DCu$ ”), and directly from the
436 2D-S data (black). Probability density functions (pdfs) of 94 GHz effective radar reflectivity match because they
437 are forced to by the two instrument parameterizations. Otherwise, biases exist between the two sets of computations
438 based on simulated instruments and computations based on the actual 2D-S (black curve). This bias is due mainly to
439 the temperature parameterization of D_m . The pdfs of extinction coefficient and IWC for the two parameterized
440 instruments match one another quite well (the differences in their medians are not statistically significant).
441 However, for N_T , the $x2DCu$ pdf is shifted to higher concentrations than the pdf for $x2DS$. The difference in their
442 medians is statistically significant at the 95% level according to a Mann-Whitney U test. It is therefore concluded
443 that the older D05 parameterization based on the 2DC-2DP data sets predicts a statistically significant higher
444 number of total ice crystals than does the parameterized 2D-S (by a factor of about 1.3, or a little over 1 dB) and
445 that, more generally, the 2DC measures a larger ratio of small ice crystals to large ice crystals than does the 2D-S, as
446 shown in the effective radius comparison in Fig. 8.

447 Figure 14 shows pdfs of N_T and extinction coefficient computed using the fully parameterized 2D-S (red,
448 labeled “ $x2DS$ ”), the fully parameterized (corrected) 2DC-2DP (blue, labeled “ $x2DCs$ ”), and directly from the 2D-S
449 data (black). The pdfs of extinction match quite well, but their medians are significantly different according to the U
450 test. The medians of N_T are also significantly different, but the mean of the parameterized, corrected 2DC is lower
451 than that of the parameterized 2D-S. A posteriori shatter correction has made 2DC measurements more like 2D-S
452 measurements in the bulk quantity of total particle concentration, however, a statistically significant difference
453 between the 2D-S and the corrected 2DC remains. This result is entirely expected in light of the previous results
454 outlined in the introduction to this paper.

455 In this paper, an indirect comparison to older, 2DC-based datasets by means of parameterizations given in
456 D05 and in D14 has been made. The main discussion points and some sources of uncertainty are now enumerated.

457 1) It is determined that the 2D-S cirrus cloud datasets used here are significantly different from historical
458 datasets in numbers of small ice crystals measured. With a posteriori shattered particle removal applied to

459 older 2DC data, the total numbers of ice crystals measured by the 2D-S and the 2DC become more similar,
460 but NT measured by the 2DC remains statistically different from that measured by the 2D-S.

- 461 2) Given the modest differences found here between bulk cirrus properties derived from PSDs, we conclude
462 that historical data sets continue to be useful. It would seem that for the measurement of bulk cirrus
463 properties—excepting N_T —instrument improvements may have produced only marginal improvements.
- 464 3) It is surmised that, since the efficacy of a posteriori shatter correction on the 2DC is questionable and since
465 the 2D-S is superior in response time, resolution, and sample volume to the 2DC, and since steps were
466 taken to mitigate ice particle shattering on the 2D-S data, that the newer data sets are more accurate.
467 Therefore, continuing large-scale field investigations of cirrus clouds using newer particle probes and data
468 processing techniques is recommended. Where possible, investigation of the possibility of statistical
469 comparison and correction of historical cirrus ice particle datasets using newer datasets by flying 2DC
470 probes alongside 2D-S and other, more advanced probes is strongly encouraged.

471 4) There are some sources of uncertainty.

- 472 a. There exists a large amount of uncertainty in mass- and density-dimensional relationships for ice
473 crystals, such as those used in D05, D14, and in this paper. In making a comparison, the best that
474 could be done was to use the same relations in this paper as in D05 and D14. This, of course—
475 depending on which part of the comparison is considered—assumes either that the same overall
476 mix of particles habits was encountered between D05 and this study and between D14 and this
477 study.
- 478 b. The data for both D05 and D14 is stated to begin at 25 μm , whereas the 2D-S data used here is
479 truncated to begin at 15 μm . This means that the 2D-S data had the potential of measuring greater
480 numbers of small particles than did the 2DC, and yet the differences in small particles between
481 D05 and the current study were still realized.
- 482 5) Finally, it is important to note that this study does not specifically consider PSD shape. [\(For a more](#)
483 [detailed discussion on cirrus PSD shape and on the efficacy of the gamma distribution, please refer to](#)
484 [Schwartz \[2014\].\)](#) This is a critical component of the answers to Korolov et al.'s (2013b) original two
485 questions. Mitchell et al. (2011) demonstrated that for a given effective diameter and IWC, the optical
486 properties of a PSD are sensitive to its shape. Therefore, PSD bimodality and concentrations of small ice

487 crystals are critical to realistically parameterizing, cirrus PSDs, to modeling their radiative properties and
488 sedimentation velocities, and to mathematical forward models designed to infer cirrus PSDs from remote
489 sensing observations (Lawson et al., 2010; Mitchell et al, 2011; Lawson, 2011). In order to improve
490 knowledge on PSD shape, as well as to develop statistical algorithms for correcting historical PSD datasets
491 so that PSD shapes are corrected along with computations of bulk properties, it will be necessary to make
492 use of instruments that can provide reliable measurements of small ice crystals beneath the size floors of
493 both the 2DC and the 2D-S. Recent studies such as Gerber and DeMott (2014) have provided aspherical
494 correction factors for particle volumes and effective diameters measured by the FSSP. However, the author
495 expects that this problem will ultimately be resolved by the continued technological development of new
496 probes such as the HOLODEC.

497 **Data Availability**

498 All SPartICus data may be accessed via the Atmospheric Radiation Measurement (ARM) data archive as
499 noted in the references. All MACPEX and TC⁴ data may be accessed from the NASA Earth Science Project Office
500 (ESPO) data archive, also noted in the references.

501 **ACKNOWLEDGEMENTS**

502 The author gratefully acknowledges the SPartICus, MACPEX, and TC⁴ science teams for the collection of
503 data used in this study. TC⁴ and MACPEX data were obtained from the NASA ESPO archive, which may be
504 accessed online at <https://espoarchive.nasa.gov/archive/browse/>. The SPartICus data were obtained from DOE
505 ARM archive and may be accessed online at
506 <http://www.archive.arm.gov/discovery/#v/results/s/fiop::aaf2009Sparticus>. In particular, the author acknowledges
507 Dr. Paul Lawson and SPEC, Inc. for all 2D-S data collected in the field, to Dr. Andrew Heymsfield for the PIP data
508 used from TC⁴, and to Dr. Linnea Avallone for CLH data used from MACPEX. Thanks are furthermore given to
509 Drs. Gerald G. Mace, Paul Lawson, and Andrew Heymsfield for helpful discussions that led to significant
510 improvements in the manuscript. This work was supported by the U.S. Department of Energy's (DOE) Atmospheric
511 System Research (ASR), an Office of Science, Office of Biological and Environmental Research (BER) program,
512 under Contract DE-AC02-06CH11357 awarded to Argonne National Laboratory. This work was also supported by
513 the National Science Foundation (NSF) Grant AGS-1445831. Grateful acknowledgement is also given to the
514 computing resources provided on Blues, a high-performance computing cluster operated by the

515 Laboratory Computing Resource Center (LCRC) at the Argonne National Laboratory.

516 **Competing Interests**

517 The author declares that he has no conflict of interest.

518 **REFERENCES**

- 519 Bain, L. J. and M. Englehardt, 1992: *Introduction to Probability and Mathematical Statistics*,
 520 *2nd Ed.* Duxbury Press, 644 pp.
 521
- 522 Baker, B. A. and R. P. Lawson, 2006: Improvement in determination of ice water content from
 523 two-dimensional particle imagery. Part I: Image-to-mass relationships. *J. Appl. Meteor. Climatol.*, **45**,
 524 1282-1290.
 525
- 526 Baumgardner, D., 1989: Airborne Measurements for Cloud Microphysics. *Res. Aviat. Facility*
 527 *Bull.*, **24**, 1-22.
 528
- 529 [Baumgardner, D., H. Jonsson, W. Dawson, D. O'Connor, and R. Newton, 2001: The cloud, aerosol and](#)
 530 [precipitation spectrometer \(CAPS\): A new instrument for cloud investigations. *Atmos. Res.*, **59-60**, 251-](#)
 531 [264, doi:10.1016/S0169-8095\(01\)00119-3.](#)
 532
- 533 [Baumgardner, D., and Coauthors, 2011: Airborne instruments to measure atmospheric aerosol particles, clouds and](#)
 534 [radiation: A cook's tour of mature and emerging technology. *Atmos. Res.*, **101**, 10-29,](#)
 535 [doi:10.1016/j.atmosres.2011.06.021.](#)
 536
- 537 [Baumgardner, D. and Coauthors, 2017: In situ measurement challenges. *Ice Formation and Evolution in Clouds*](#)
 538 [and *Precipitation: Measurement and Modeling Challenges*, Meteor. Monogr., No. 58, Amer. Meteor. Soc.,](#)
 539 [doi:10.1175/AMSMONOGRAPHIS-D-16-0011.1.](#)
 540
- 541 [Breguier, J.-L., Bachalo, W. D., Chuang, P. Y., Esposito, B. M., Fugal, J., Garrett, T., Gayet, J.-F., Gerber, H.,](#)
 542 [Heymsfield, A., Kokhanovsky, A., Korolev, A., Lawson, R. P., Rogers, D. C., Shaw, R. A., Strapp, W. and](#)
 543 [Wendisch, M. \(2013\) *In Situ Measurements of Cloud and Precipitation Particles*, in *Airborne*](#)
 544 [Measurements for Environmental Research: Methods and Instruments \(eds M. Wendisch and J.-L.](#)
 545 [Breguier\), Wiley-VCH Verlag GmbH & Co. KGaA, Weinheim, Germany.](#)
 546 [doi: 10.1002/9783527653218.ch5](#)
 547
- 548 Brown, P. R. A., and P. N. Francis, 1995: Improved Measurements of the Ice Water Content in
 549 Cirrus Using a Total Water Probe. *J. Atmos. Oceanic Technol.*, **12**, 410-414.
 550
- 551 Cooper, W. A., 1978: Cloud physics investigations by the University of Wyoming in HIPLEX
 552 1977. Department of Atmospheric Science, University of Wyoming, Rep. AS119, 320 pp.
 553
- 554 Davis, S. M., A. G. Hallar, L. M. Avallone, and W. Engblom, 2007: Measurements of Ice Water
 555 Content With a Tunable Diode Laser Hygrometer: Calibration Procedure and Inlet Analysis. *J. Atmos.*
 556 *Oceanic Technol.*, **24**, 463, doi:10.1175/JTECH1975.1.
 557
- 558 Delanoë, J., A. Protat, J. Testud, D. Bouniol, A. J. Heymsfield, A. Bansemmer, P. R. A. Brown,
 559 and R. M. Forbes, 2005: Statistical properties of the normalized ice particle size distribution. *J. Geophys.*
 560 *Res.*, **110**, doi:10.1029/2004JD005405.
 561
- 562 Delanoë, J. M. E., A. J. Heymsfield, A. Protat, A. Bansemmer, and R. J. Hogan, 2014: Normalized
 563 particle size distribution for remote sensing application. *J. Geophys. Res.*, **119**,
 564 doi:10.1002/2013JD020700.
 565
- 566 Demortier, Luc, 1995: Assessing the Significance of a Deviation in the Tail of a Distribution.
 567 Collider Detector at Fermilab note 3419.
 568
- 569 Field, P. R., 2000: Bimodal ice spectra in frontal clouds. *Quart. J. Roy. Meteor. Soc.*, **126**, 379-
 570 392.
 571
- 572 Field, P. R., R. Wood, P. R. A. Brown, P. H. Kay, E. Hirst, R. Greenaway, and J. A. Smith,

573 2003: Ice Particle Interarrival Times Measured with a Fast FSSP. *J. Atmos. Oceanic Technol.*, **20**, 249-
574 261.
575
576 Field, P. R., R. J. Hogan, P. R. A. Brown, A. J. Illingworth, T. W. Choulaton, and R. J. Cotton,
577 2005: Parameterization of ice-particle size distributions for mid-latitude stratiform cloud. *Quart. J. Roy.*
578 *Meteor. Soc.*, **131**, 1997-2017.
579
580 Field, P. R., A. J. Heymsfield, and A. Bansemmer, 2006: Shattering and particle interarrival times
581 measured by optical array probes in ice clouds. *J. Atmos. Oceanic Technol.*, **23**, 1357-1371.
582
583 [Fugal, J., and R. Shaw, 2009: Cloud particle size distributions measured with an airborne digital in-line holographic](#)
584 [instrument. *Atmos. Meas. Tech.*, **2**, 259-271, doi:10.5194/amt-2-259-2009.](#)
585
586 [Garrett, T. J., H. Gerbert, D.G. Baumgardner, C.H. Twohy, and E.M. Weinstock, 2003: Small, highly reflective ice](#)
587 [crystals in low-latitude cirrus. *Geophys. Res. Lett.*, **30**, doi:10.1029/2003GL018153.](#)
588
589 Gayet, J.-F., F. Auriol, A. Minikin, J. Stroem, M. Seifert, R. Krejci, A. Petzold, G.
590 Febvre, and U. Schumann, 2002: Quantitative measurement of the microphysical and optical properties of
591 cirrus clouds with four different in situ probes: Evidence of small ice crystals. *Geophys. Res. Lett.*, **29**,
592 doi:10.1029/2001GL014342.
593
594 Gayet, J.-F., J. Ovarlez, V. Shcherbakov, J. Stroem, U. Schumann, A. Minikin, F. Auriol,
595 A. Petzold, and M. Monier, 2004: Cirrus cloud microphysical and optical properties at southern and
596 northern midlatitudes during the INCA experiment. *J. Geophys. Res.*, **109**, D20206,
597 doi:10.1029/2004JD004803.
598
599 Gayet, J.-F., V. Shcherbakov, H. Mannstein, A. Minikin, U. Schumann, J. Stroem, A.
600 Petzold, J. Ovarlez, and F. Immler, 2006: Microphysical and optical properties of midlatitude cirrus
601 clouds observed in the southern hemisphere during INCA. *Quart. J. Roy. Meteor. Soc.*, **132**, 2719-2748.
602
603 [Gerber, H. and P. J. DeMott, 2014: Response of FSSP-100 and PVM-100A to Small Ice Crystals. *J. Atmos.*](#)
604 [Oceanic Technol.](#), **31**, 2145-2155, doi:10.1175/JTECH-D-13-00228.1.
605
606 Gurganus, C. and P. Lawson, 2016: Improvements in Optical Array Probe Characterization:
607 Laboratory and Simulation Results. *XVII International Conference on Clouds and Precipitation*,
608 Manchester, UK, the International Association of Meteorology and Atmospheric Sciences and the
609 International Commission on Clouds and Precipitation.
610
611 Hammonds, K. D., G. G. Mace, and S. Y. Matrosov, 2014: Characterizing the Radar
612 Backscatter-Cross-Section Sensitivities of Ice-Phase Hydrometeor Size Distributions via a Simple Scaling
613 of the Clausius-Mossotti Factor. *J. Appl. Meteor. Climatol.*, **53**, 2761-2774.
614
615 [Heymsfield, A. J., and G. M. McFarquhar, 1996: High albedos of cirrus in the tropical Pacific warm pool:](#)
616 [Microphysical interpretations from CEPEX and from Kwajalein, Marshall Islands. *J. Atmos. Sci.*, **53**,](#)
617 [2424-2451, doi:10.1175/1520-0469\(1996\)053<2424:HAOCIT>2.0.CO;2.](#)
618
619 Heymsfield, A. J., A. Bansemmer, P. R. Field, S. L. Durden, J. L. Stith, J. E. Dye, W. Hall, and C.
620 A. Grainger, 2002: Observations and Parameterizations of Particle Size Distributions in Deep Tropical
621 Cirrus and Stratiform Precipitating Clouds: Results from In Situ Observations in TRMM Field Campaigns.
622 *J. Atmos. Sci.*, **59**, 3457-3491.
623
624 Heymsfield, A. J., 2003: Properties of Tropical and Midlatitude Ice Cloud Particle Ensembles.
625 Part I: Median Mass Diameters and Terminal Velocities. *J. Atmos. Sci.*, **60**, 2573-3591.
626
627 Heymsfield, A. J., A. Bansemmer, G. Heymsfield, and A. O. Fierro, 2009: Microphysics of
628 Maritime Tropical Convective Uprrafts at Temperatures from -20° to -60°C. *J. Atmos. Sci.*, **66**, 3530-3562.

629
630 Heymsfield, A. J. C. Schmitt, A. Bansemer, and C. H Twohy, 2010: Improved representation of
631 ice particle masses based on observations in natural clouds, *J. Atmos. Sci.*, **67**, 3303-3318,
632 doi:10.1175/2010JAS3507.1
633
634 [Heymsfield, A.J., M. Krämer, A. Luebke, P. Brown, D.J. Cziczo, C. Franklin, P. Lawson, U. Lohmann, G.
635 McFarquhar, Z. Ulanowski, and K. Van Tricht, 2017: Cirrus Clouds. *Meteorological Monographs*, **58**, 2.1–
636 2.26, doi: 10.1175/AMSMONOGRAPHS-D-16-0010.1.](#)
637
638 Hobbs, P. V. and A. L. Rangno, 1985: Ice particle concentrations in clouds. *J. Atmos.*
639 *Sci.*, **42**, 2523–2549.
640
641 Hogan, R. J., L. Tian, P. R. A. Brown, C. D. Westbrook, A. J. Heymsfield, and J. D. Eastment,
642 2012: Radar Scattering from Ice Aggregates Using the Horizontally Aligned Oblate Spheroid
643 Approximation. *J. Appl. Meteor. Climatol.*, **51**, 655-671.
644
645 Jackson, R. C. and G. M McFarquhar, 2014: An Assessment of the Impact of Antishattering
646 Tips and Artifact Removal Techniques on Bulk Cloud Ice Microphysical and Optical Properties Measured
647 by the 2D Cloud Probe. *J. Atmos. Oceanic Technol.*, **30**, 2131-2144.
648
649 Jackson, R. C., G. M. McFarquhar, J. Stith, M. Beals, R. A. Shaw, J. Jensen, J. Fugal, and A.
650 Korolev, 2014: An Assessment of the Impact of Antishattering Tips and Artifact Removal Techniques on
651 Cloud Ice Size Distributions Measured by the 2D Cloud Probe. *J. Atmos. Oceanic Technol.*, **31**, 2576-
652 2590.
653
654 Jensen, E. J., and Coauthors, 2009: On the importance of small ice crystals in tropical anvil
655 cirrus. *Atmos. Chem. Phys.*, **9**, 5519-5537.
656
657 Johnson, R. W., D. V. Kliche, and P. L. Smith, 2013: Maximum likelihood estimation
658 of gamma parameters for coarsely-binned and truncated raindrop size data. *Quart. J. Roy. Meteor. Soc.*,
659 doi:10.1002/qj.2209.
660
661 Khain, A., M. Pinsky, T. Elperin, N. Kleeorin, I. Rogachevskii, and A. Kostinski, 2007:
662 Critical comments to results of investigations of drop collisions in turbulent clouds. *Atmospheric Research*,
663 **86**, 1–20.
664
665 [Knollenburg, R., 1976: Three new instruments for cloud physics measurements: The 2-D spectrometer probe, the
666 forward scattering spectrometer probe, and the active scattering aerosol spectrometer. Preprints, *Int. Conf.*
667 *on Cloud Physics*, Boulder, CO, Amer. Meteor. Soc., 554-561.](#)
668
669 [Knollenburg, R., 1981: Techniques for probing cloud microstructure. *Clouds, Their Formation, Optical Properties*
670 *and Effects*, P. V. Hobbs and A. Deepak, Eds., Academic Press, 15-91.](#)
671
672 Korolev, A. V. and G. Isaac, 2003: Roundness and Aspect Ratio of Particles in Ice Clouds. *J.*
673 *Atmos. Sci.*, **60**, 1795-1808.
674
675 Korolev, A. V., E. F. Emery, J. W. Strapp, S. G. Cober, G. A. Isaac, M. Wasey, and D. Marcotte,
676 2011: Small Ice Particles in Tropospheric Clouds: Fact or Artifact?. *Bull. Amer. Meteor. Soc.*, **92**, 967-
677 973.
678
679 Korolev, A., E. Emery, and K Creelman, 2013a: Modification and Tests of Particle Probe Tips
680 to Mitigate Effects of Ice Shattering. *J. Atmos. Oceanic Technol.*, **30**, 690-708.
681
682 Korolev, A. V., E. F. Emerty, J. W. Strapp, S. G. Cober, and G. A. Isaac, 2013b: Quantification
683 of the effects of Shattering on Airborne Ice Particle Measurements. *J. Atmos. Oceanic Technol.*, **30**, 2527-
684 2553.

685
686 Korolev, A., and P. R. Field, 2015: Assessment of the performance of the inter-arrival time
687 algorithm to identify ice shattering artifacts in cloud particle probe measurements. *Atmos. Meas. Tech.*, **8**,
688 761-777.
689
690 Kostinski, A. B., and R. A. Shaw, 2001: Scale-dependent droplet clustering in turbulent
691 clouds. *J. Fluid. Mech.*, **434**, 389–398.
692
693 Lance, S., C. A. Brock, D. Rogers, and J. A. Gordon, 2010: Water droplet calibration of the cloud droplet probe
694 (CDP) and in-flight performance in liquid, ice and mixed-phase clouds during ARCPAC. *Atmos. Meas.*
695 *Tech.*, **3**, 1683-1706, doi:10.5194/amt-3-1683-2010.
696
697 Lawson, R. P., R. E. Stewart, and L. J. Angus, 1998: Observations and numerical simulations of the origin and
698 development of very large snowflakes. *J. Atmos. Sci.*, **55**, 3209-3229, doi:10.1175/1520-
699 0469(1998)055<3209:OANSOT>2.0.CO;2.
700
701 Lawson, R. P., B. Baker, B. Pilson, and Q. Mo, 2006: In Situ Observations of the
702 Microphysical Properties of Wave, Cirrus, and Anvil Clouds. Part II: Cirrus Clouds. *J. Atmos. Sci.*, **63**,
703 3186-3203.
704
705 Lawson, R. P., E. Jensen, D. L. Mitchell, B. Baker, Q. Mo, and B. Pilson, 2010: Microphysical
706 and radiative properties of tropical clouds investigated in TC4 and NAMMA. *J. Geophys. Res.*, **115**,
707 doi:10.1029/2009JD013017.
708
709 Lawson, R. P., 2011: Effects of ice particles shattering on the 2D-S probe. *Atmos. Meas.*
710 *Tech.*, **4**, 1361–1381.
711
712 Locatelli, J. D., and P. V. Hobbs, 1974: Fall speed and masses of solid precipitation particles. *J.*
713 *Geophys. Res.*, **79**, 2185-2197.
714
715 MACPex Science Team, 2011: MACPEX. NASA Earth Science Project Office Data Archive, accessed 31 March
716 2013. [Available online at <https://espoarchive.nasa.gov/archive/browse/macpex>.]
717
718 Matrosov, S. Y., 2007: Modeling Backscatter Properties of Snowfall at Millimeter Wavelengths.
719 *J. Atmos. Sci.*, **64**, 1727-1736.
720
721 Matrosov, S. Y., G. G. Mace, R. Marchand, M. D. Shupe, A. G. Hallar, and I. B. McCubbin,
722 2012: Observations of Ice Crystal Habits with a Scanning Polarimetric W-Band Radar at Slant Linear
723 Depolarization Ratio Mode. *J. Atmos. Oceanic Technol.*, **29**, 989-1008.
724
725 McFarquhar, G. M., J. Um, M. Freer, D. Baumgardner, G. L. Kok, and G. Mace, 2007:
726 Importance of small ice crystals to cirrus properties: Observations from the Tropical Warm Pool
727 International Cloud Experiment (TWP-ICE). *Geophys. Res. Lett.*, **34**, doi:10.1029/2007GL029865.
728
729 Meakin, P., 1992: Aggregation kinetics. *Physica Scripta*, **46**, 295–331.
730
731 Mitchell, D. L., R. P. Lawson, and B. Baker, 2011: Understanding effective diameter and its
732 application to terrestrial radiation in ice clouds. *Atmos. Chem. Phys.*, **11**, 3417-3429.
733
734 Moon, T. K., 1996: The Expectation-Maximization Algorithm. *IEEE Signal Processing*
735 *Magazine*, **13**, 47-60.
736
737 Petty, G. W. and W. Huang, 2011: The Modified Gamma Size Distribution Applied to
738 Inhomogenous and Nonspherical Particles: Key Relationships and Conversions. *J. Atmos. Sci.*, **68**, 1460-
739 1473.
740

741 Pinsky, M. and A. Khain, 2003: Fine structure of cloud droplet concentration as seen
742 from the Fast-FSSP measurements. Part II: Results of in situ observations. *J. Appl. Meteor. Climatol.*, **42**,
743 65–73.
744

745 Posselt, D. and G. G. Mace, 2013: The Influence of Parameter Uncertainty on Snowfall
746 Retrievals Using Markov Chain Monte Carlo Solution Methods. *J. Appl. Meteor. Climatol.*, Accepted.
747

748 Schwartz, M. C., 2014: Analysis of Cirrus Particle Size Distributions from Three In Situ Flight
749 Campaigns: Applications to Cirrus Microphysics and Parameterization, Remote Sensing, and Radar
750 Forward Model Simulators. Ph.D. dissertation, Dept. of Atmospheric Sciences, the University of Utah, 229
751 pp.
752

753 SPartICus Science Team, 2010: SPartICus. Atmospheric Radiation Measurement Data Archive, PI/Campaign Data,
754 accessed 26 March 2013. [Available online at
755 <http://www.archive.arm.gov/discovery/#v/results/s/fiop::aaf2009Sparticus.>]
756

757 TC⁴ Science Team, 2007: TC4 DC-8 files. NASA Earth Science Project Office Data Archive, accessed 29 March
758 2012. [Available online at <https://espoarchive.nasa.gov/archive/browse/tc4/DC8.>]
759

760 Tinel, C., J. Testud, J. Pelon, R. J. Hogan, A. Protat, J. Delanoe, and D. Bouniol, 2005:
761 The retrieval of ice-cloud properties from cloud radar and lidar synergy. *J. Appl. Meteor.*, **44**, 860–875.
762

763 [Ulanowski, Z., P. H. Kaye, E. Hirst, R. S. Greenaway, R. J. Cotton, E. Hesse, and C. T. Collier, 2014: Incidence of](#)
764 [rough and irregular atmospheric ice particles from Small Ice Detector 3 measurements. *Atmos. Chem.*](#)
765 [Phys., **14**, 1649-1662, doi:10.5194/acp-14-1649-2014.](#)
766

767 Vidaurre, G. and J. Hallett, 2009: Particle Impact and Breakup in Aircraft Measurement. *J.*
768 *Atmos. Oceanic Technol.*, **26**, 972-983.
769

769 Westbrook, C. D., R. C. Ball, P. R. Field, and A. J. Heymsfield, 2004a: Universality in
770 snowflake aggregation. *Geophys. Res. Lett.*, **31**, L15104, doi:10.1029/2004GL020363.
771

772 Westbrook, C. D., R. C. Ball, P. R. Field, and A. J. Heymsfield, 2004b: Theory of growth by
773 differential sedimentation, with application to snowflake formation. *Physical Review E*, **70**, 021403,
774 doi:10.1103/PhysRevE.70.021403.
775

776 Wilks, D. S., 2006: *Statistical Methods in the Atmospheric Sciences*, 2nd Ed. Academic Press,
777 627 pp.
778

779 Zhao, Y., G. G. Mace, and J. M. Comstock, 2011: The occurrence of particle size
780 distribution bimodality in midlatitude cirrus as inferred from ground-based remote sensing data. *J. Atmos.*
781 *Sci.*, **68**, 1162–1176.
782

783 **FIGURE CAPTIONS**

784

785 | [Figure 1: Flowchart illustrating the method of comparison between parameterized shatter-corrected 2DC/2DP](#)
786 [dataset, uncorrected 2DC/2DP dataset, and shatter-corrected 2D-S dataset.](#)

787

788 | [Figure 2:](#) Comparisons of computed and measured total number concentration for 15-second PSD averages and for
789 truncation of none through the first two PSD size bins.

790

791 | [Figure 3:](#) Histograms of normalized PSDs from each flight campaign, overlaid with their mean, normalized PSDs
792 (D05 normalization). The color map is truncated at 75% of the highest number of samples in a bin so as to increase
793 contrast. (a) TC⁴ (b) MACPEX (c) SPaRtICus (d) all data combined

794 | [Figure 4:](#) The mean, normalized PSD (D05 normalization) from all three datasets combined, overlaid with two
795 parameterizations from D05: the gamma-mu parameterization (dash-dotted curve) and the modified gamma
796 parameterization (dashed curve). Panel (b) is a zoom-in on a portion of panel (a).

797 | [Figure 5:](#) Same as [Figure 3](#), but using D14 normalization.

798 | [Figure 6:](#) The mean, normalized PSD (D14 normalization) from all three datasets combined, overlaid with the
799 parameterizations from D14. Panel (b) is a zoom-in on a portion of panel (a).

800

801 | [Figure 7:](#) Total number concentration computed using the parameterized universal PSDs from D05 along with true
802 values of N_0^* and D_m (from the 2D-S data) scattered vs. total number concentration computed directly from
803 untransformed 2D-S data.

804

805 | [Figure 8:](#) Mean relative error and standard deviation of the relative error between total number concentration
806 (divided by 10), effective radius, IWC, and Z as computed directly from the 2D-S and as computed from the
807 modified-gamma universal PSD shape and the true N_0^* and D_m computed from the 2D-S data. [Standard error of](#)
808 [the mean and standard deviation are shown with red error bars.](#)

809

810 | [Figure 9:](#) As in [Figure 8](#), but using the shatter-corrected 2DC parameterization.

811

812

813 | [Figure 10:](#) Data from TC⁴ alone. The mean, normalized PSD from the 2D-S is overlaid with the mean, normalized
814 PSD obtained from combining the 2D-S with the PIP and the modified gamma parameterization from D05 (dashed
815 curve). Panel (b) is a zoom-in on a portion of panel (a).

816

817 | [Figure 11:](#) Two-dimensional histogram of 94 GHz effective radar reflectivity computed, using the
818 Hammonds/Matrosov approach, from the 2D-S alone versus that computed from the 2D-S combined with the PIP.

819

820 | [Figure 12:](#) Distributions of quantities computed using the parametric modified gamma distribution along with the
821 true values of N_0^* and D_m computed from the 2D-S alone and from the 2D-S combined with the PIP. (a) N_T (b)
822 extinction coefficient (c) IWC (d) 94 GHz effective radar reflectivity

823

824 | [Figure 13:](#) Marginal pdfs of quantities computed directly from 2D-S data, as well as computed using the
825 parameterized 2D-S and the parameterized, uncorrected 2DC. (a) total number concentration (b) shortwave
826 extinction coefficient (c) ice water content (d) radar reflectivity

827

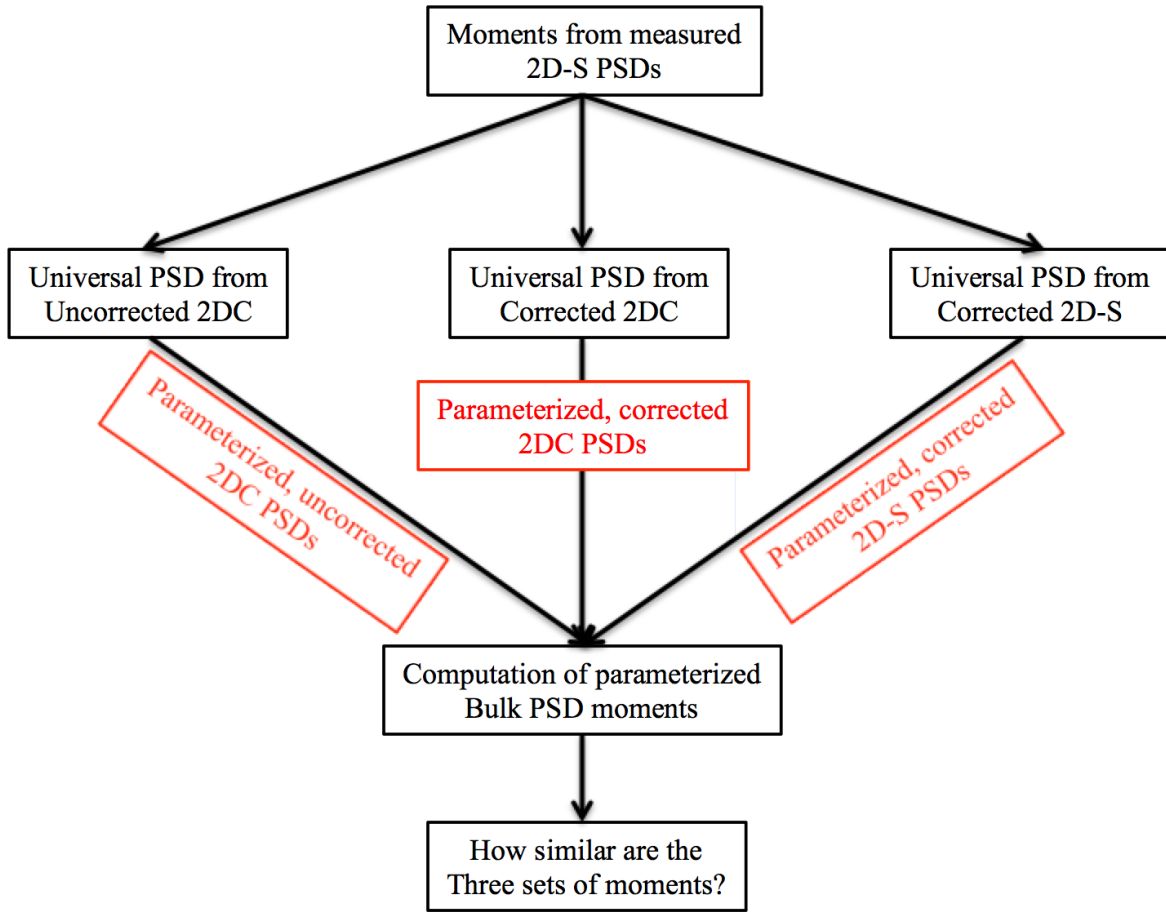
828 | [Figure 14:](#) Marginal pdfs of quantities computed directly from 2D-S data, as well as computed using the
829 parameterized 2D-S and the parameterized, corrected 2DC. (a) total number concentration (b) shortwave extinction

830

831

832
833
834

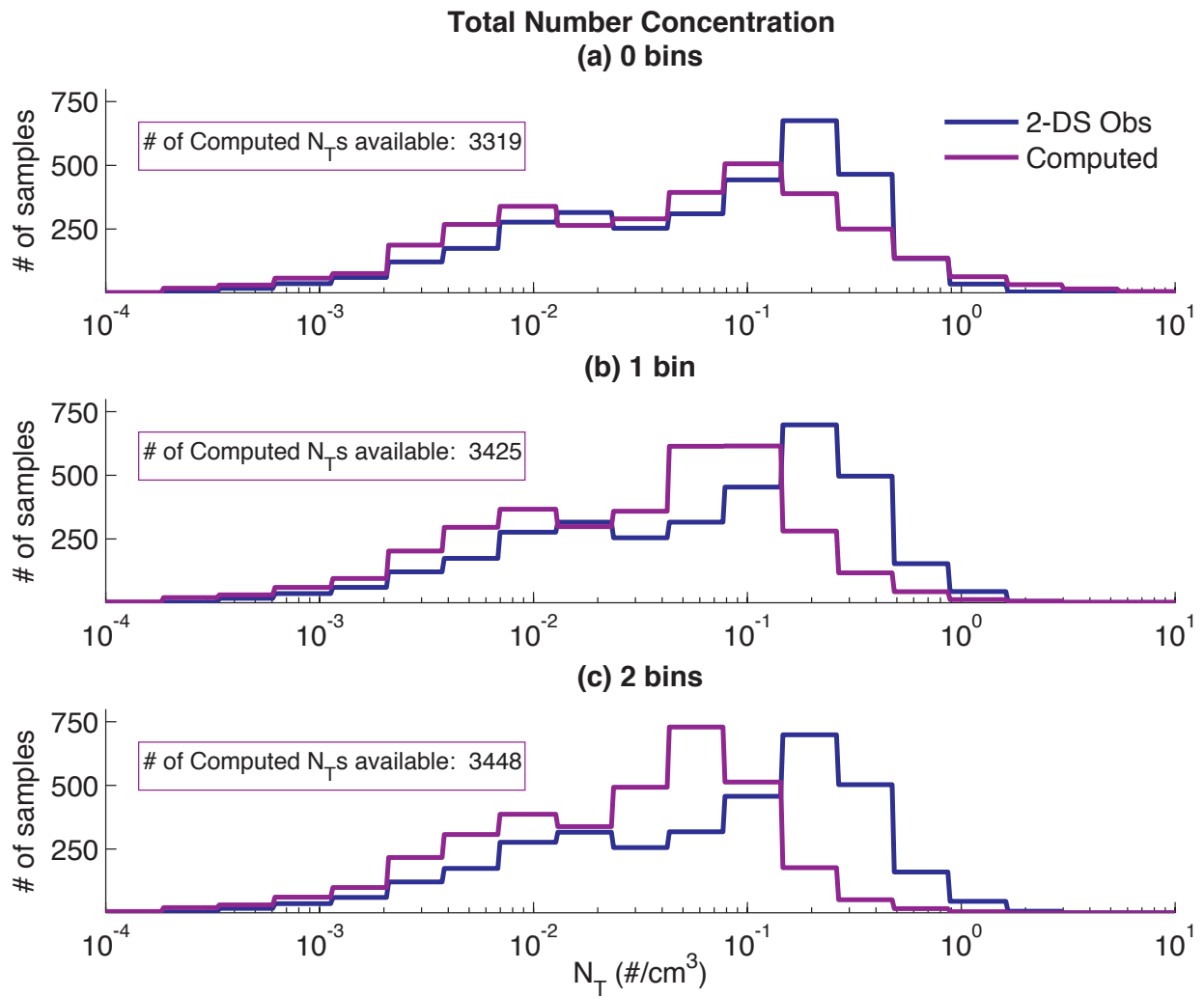
FIGURES



835
836
837
838

Figure 2: Flowchart illustrating the method of comparison between parameterized shatter-corrected 2DC/2DP dataset, uncorrected 2DC/2DP dataset, and shatter-corrected 2D-S dataset.

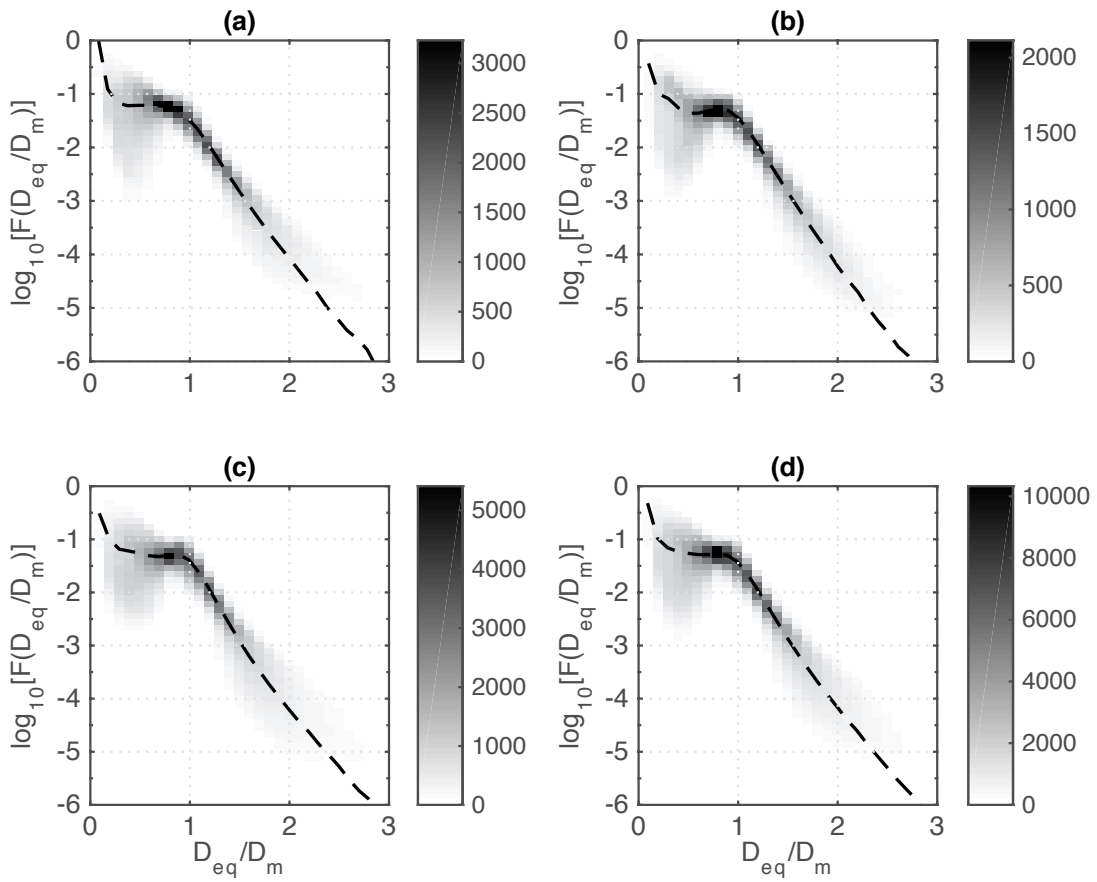
839
840
841



842
843
844

Figure 2: Comparisons of computed and measured total number concentration for 15-second PSD averages and for truncation of none through the first two PSD size bins.

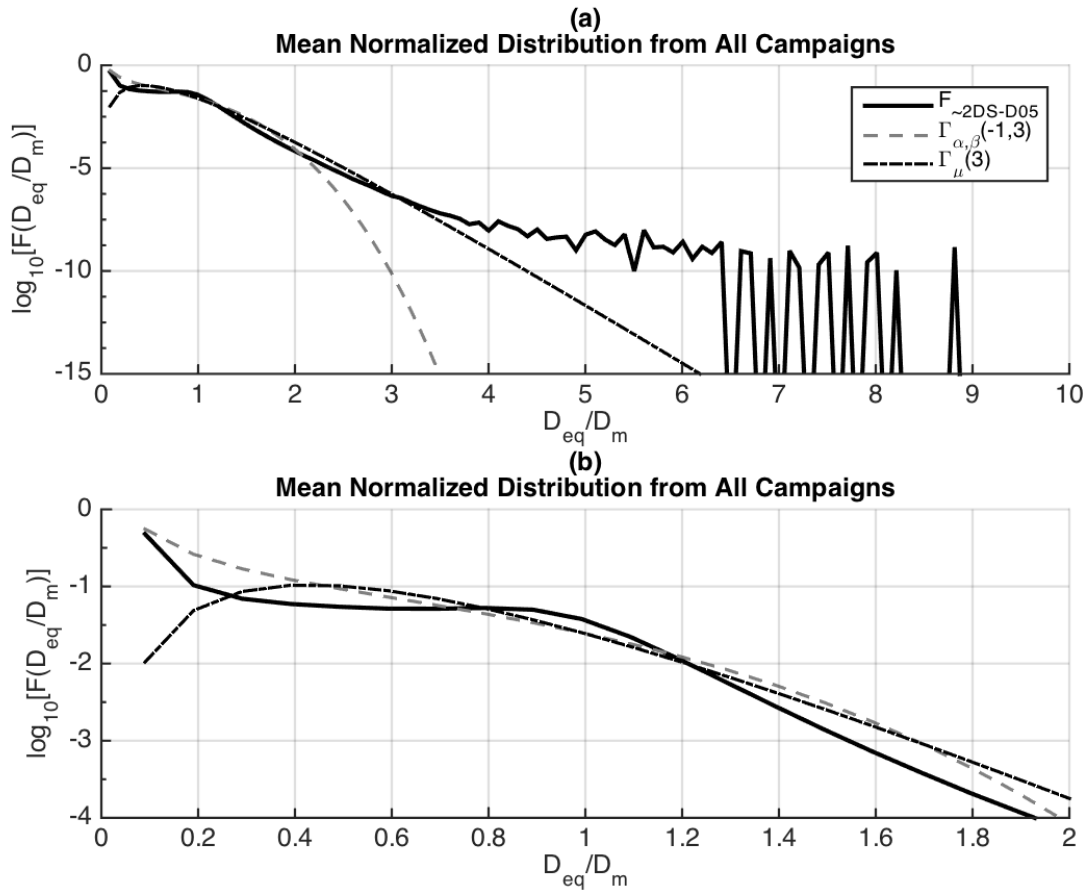
845
846



847
848
849
850

Figure 3: Histograms of normalized PSDs from each flight campaign, overlaid with their mean, normalized PSDs (D05 normalization). The color map is truncated at 75% of the highest number of samples in a bin so as to increase contrast. (a) TC⁴ (b) MACPEX (c) SPARTICUS (d) all data combined

851



852 | **Figure 4:** The mean, normalized PSD (D05 normalization) from all three datasets combined, overlaid with
 853 | two parameterizations from D05: the gamma-mu parameterization (dash-dotted curve) and the modified
 854 | gamma parameterization (dashed curve). Panel (b) is a zoom-in on a portion of panel (a).
 855 |

856

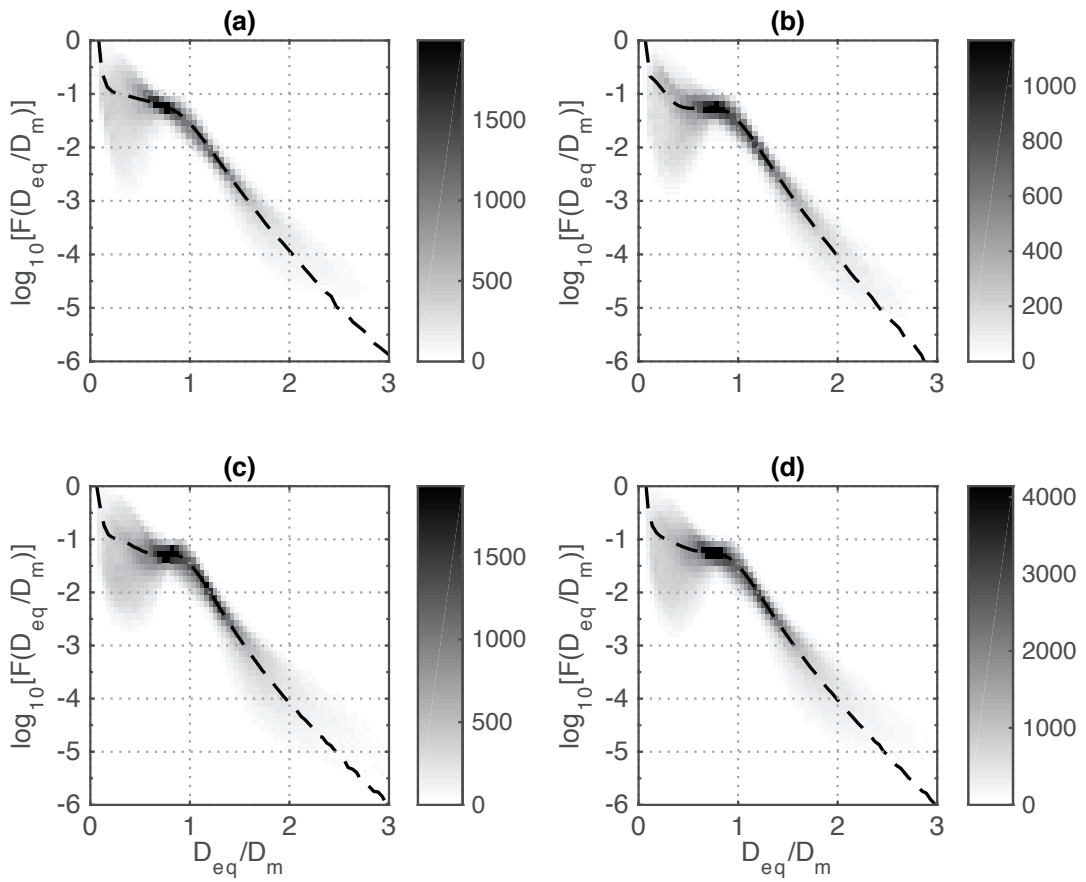
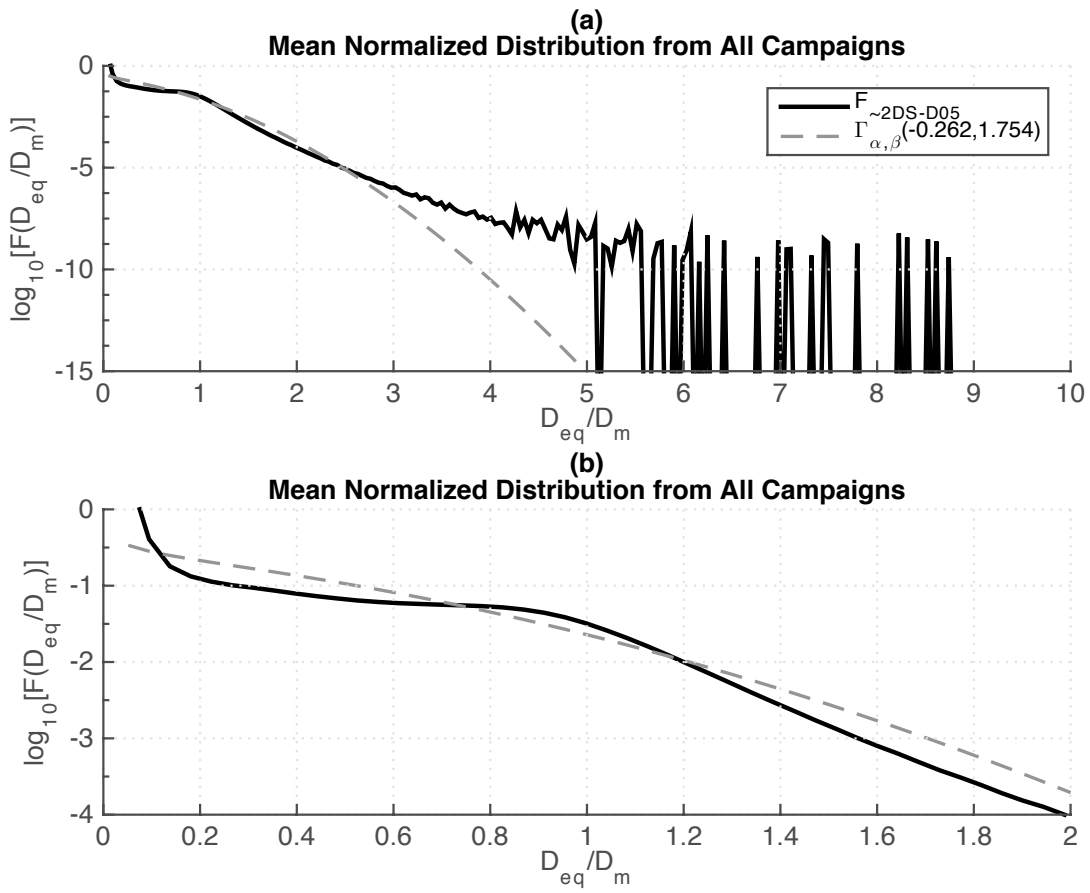


Figure 5: Same as Figure 3, but using D14 normalization.

857
858

859
860
861

862



863

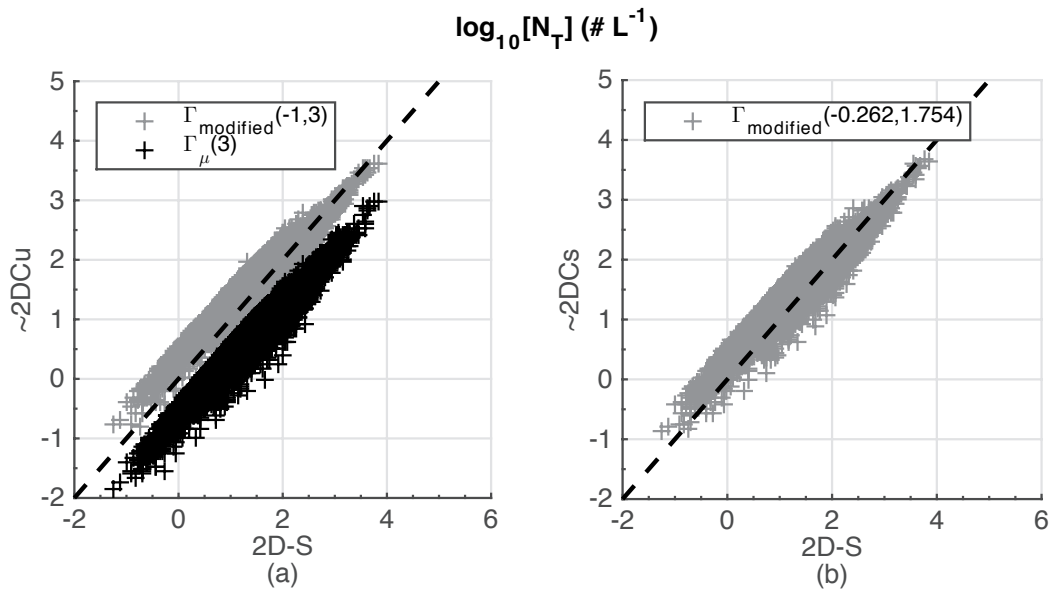
864

865

Figure 6: The mean, normalized PSD (D14 normalization) from all three datasets combined, overlaid with the parameterizations from D14. Panel (b) is a zoom-in on a portion of panel (a).

866

867



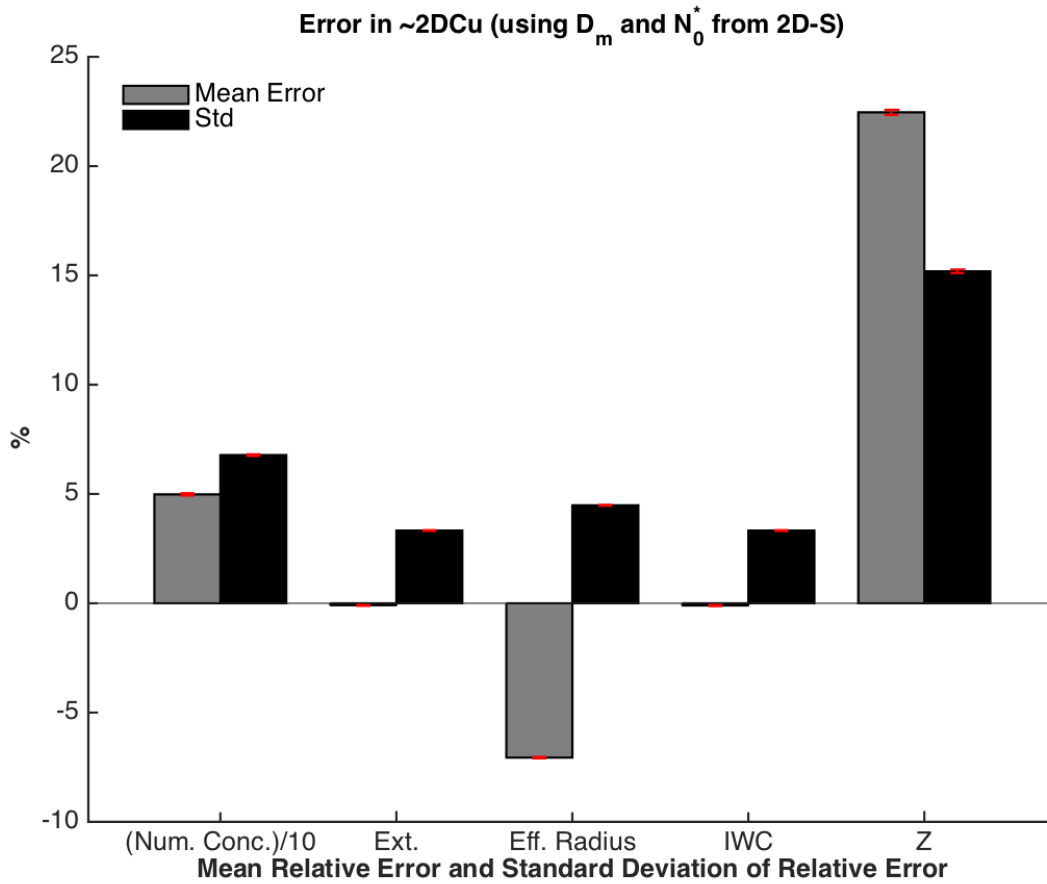
869

870 | **Figure 7:** Total number concentration computed using the parameterized universal PSDs from D05 along871 with true values of N_0^* and D_m (from the 2D-S data) scattered vs. total number concentration computed

872 directly from untransformed 2D-S data.

873

874



876

877

878

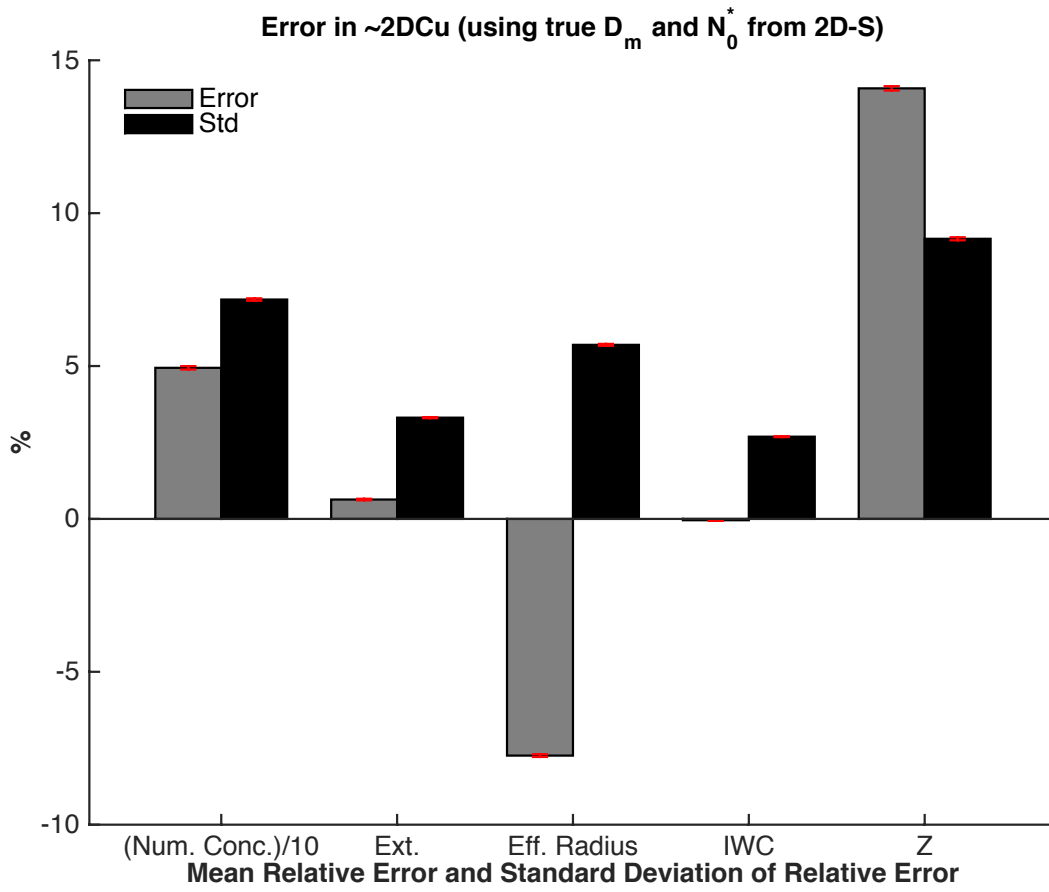
879

880

881

Figure 8: Mean relative error and standard deviation of the relative error between total number concentration (divided by 10), effective radius, IWC, and Z as computed directly from the 2D-S and as computed from the modified-gamma universal PSD shape and the true N_0^* and D_m computed from the 2D-S data. Standard error of the mean and standard deviation are shown with red error bars.

882



883

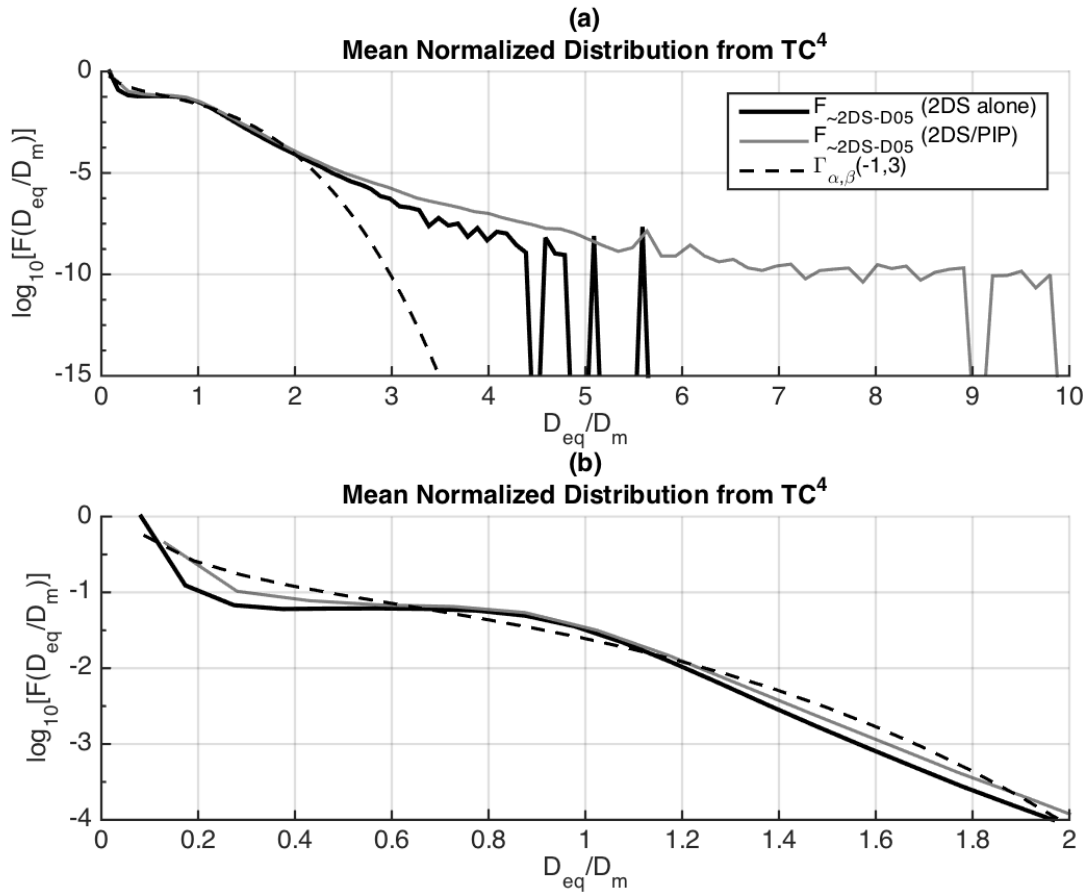
884

Figure 9: As in Figure 8, but using the shatter-corrected 2DC parameterization.

885

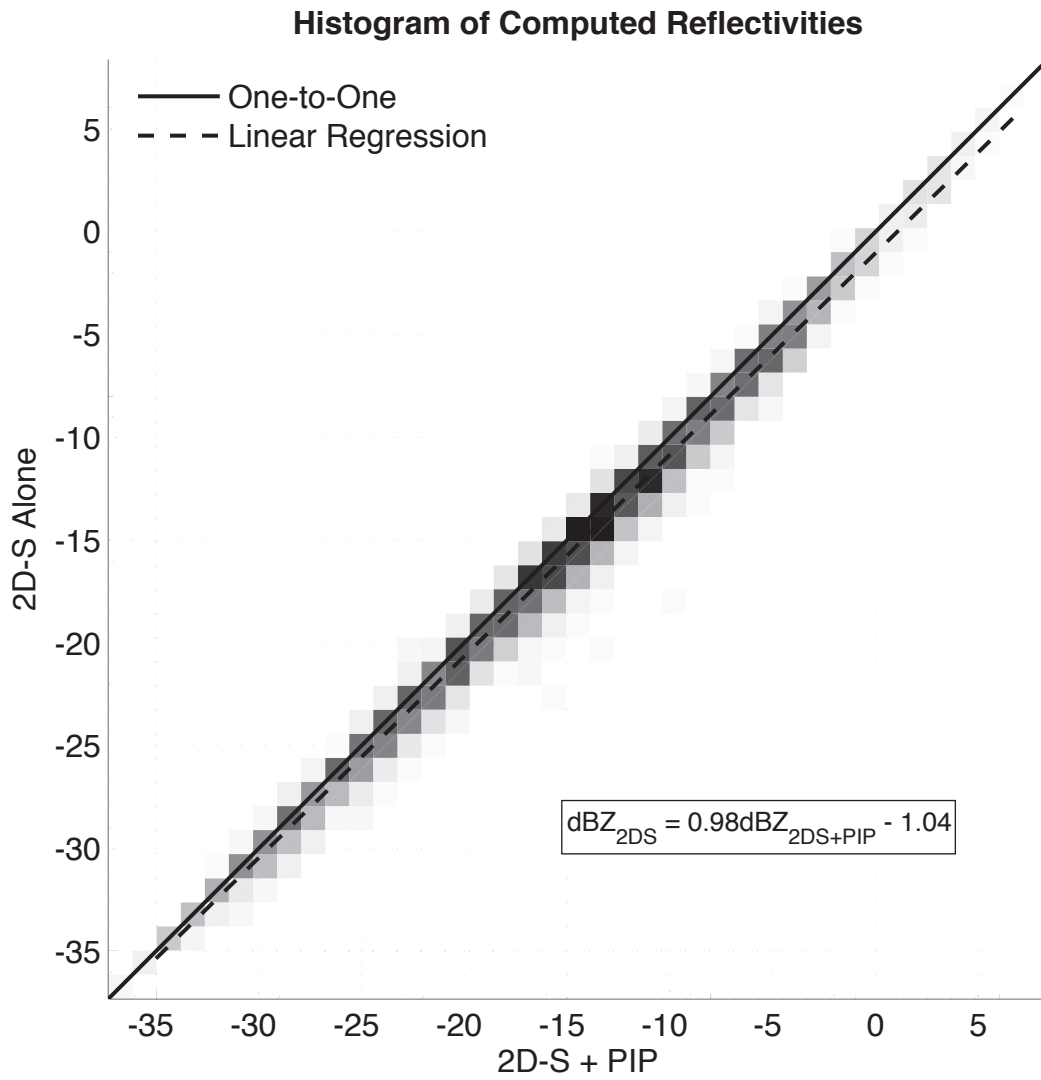
886

887
888



889
890
891
892
893

Figure 10: Data from TC⁴ alone. The mean, normalized PSD from the 2D-S is overlaid with the mean, normalized PSD obtained from combining the 2D-S with the PIP and the modified gamma parameterization from D05 (dashed curve). Panel (b) is a zoom-in on a portion of panel (a).



895

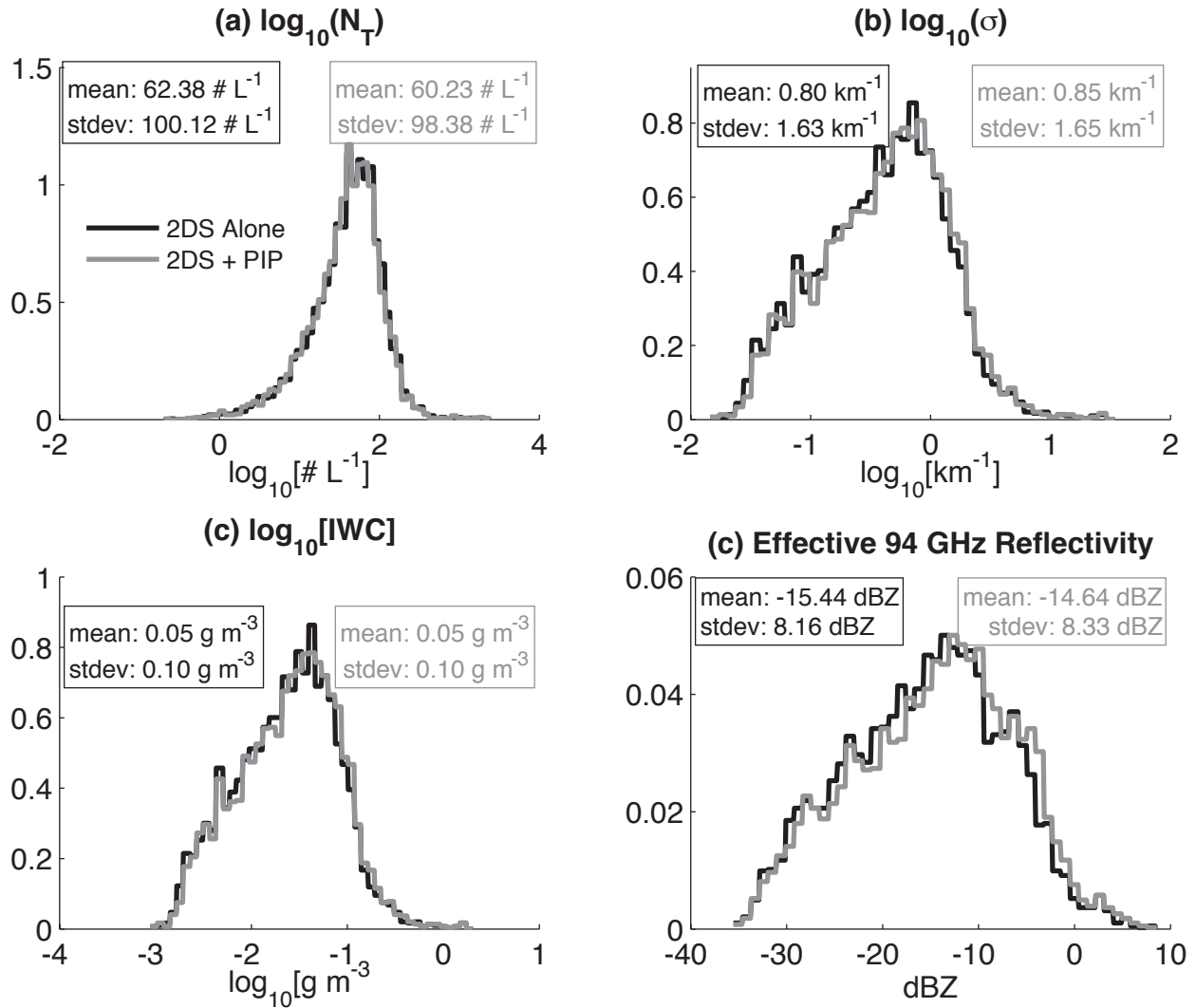
896 |

897

898

Figure 11: Two-dimensional histogram of 94 GHz effective radar reflectivity computed, using the Hammonds/Matrosov approach, from the 2D-S alone versus that computed from the 2D-S combined with the PIP.

899



900

901 | **Figure 12:** Distributions of quantities computed using the parametric modified gamma distribution along
 902 with the true values of N_0^* and D_m computed from the 2D-S alone and from the 2D-S combined with the
 903 PIP. (a) N_T (b) extinction coefficient (c) IWC (d) 94 GHz effective radar reflectivity

904

905

906

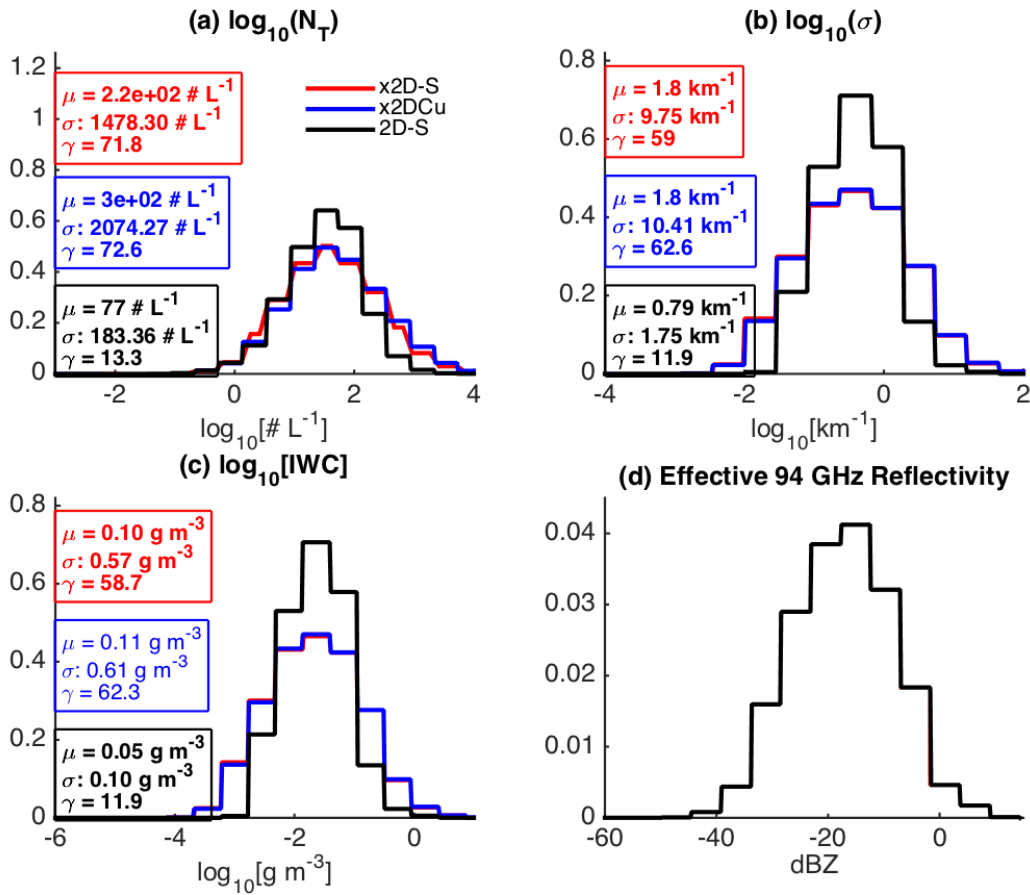
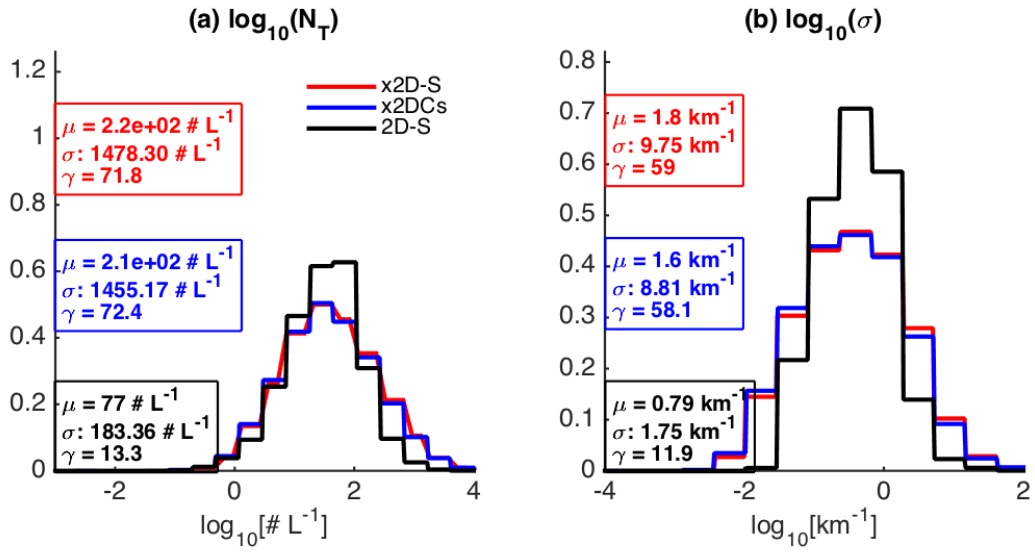


Figure 13: Marginal pdfs of quantities computed directly from 2D-S data, as well as computed using the parameterized 2D-S and the parameterized 2DC. (a) total number concentration (b) shortwave extinction coefficient (c) ice water content (d) radar reflectivity



914
915
916
917

Figure 14: Marginal pdfs of quantities computed directly from 2D-S data, as well as computed using the parameterized 2D-S and the parameterized, corrected 2DC. (a) total number concentration (b) shortwave extinction